Project Title: Low-Temperature, Anode-Supported High Power Density Solid Oxide Fuel Cells with Nanostructured Electrodes

Fourth Semiannual Technical Report

September 26, 2001 – March 26, 2002

Contract Number: DE-AC26-99FT40713

Principal Investigator: Prof. Anil V. Virkar
Department of Materials Science & Engineering
122 S. Central Campus Drive
University of Utah
Salt Lake City, UT 84112
Phone: (801) 581-5396
Fax: (801) 581-4816
Email: anil.virkar@m.cc.utah.edu

Disclaimer:

This report contains the following:

1) A manuscript, accepted for publication in the J. of the Electrochemical Society, Inc. entitled, 'Performance of Solid Oxide Fuel Cells with LSGM-LSM Composite Cathodes' by Tad J. Armstrong and Anil V. Virkar.
2) A manuscript, accepted for publication in the J. of the Electrochemical Society, Inc., entitled, 'Measurement of O_2-N_2 Effective Diffusivity in Porous Media at High Temperatures Using an Electrochemical Cell', by Feng Zhao, Tad J. Armstrong, and Anil V. Virkar

PERFORMANCE OF SOLID OXIDE FUEL CELLS WITH LSGM-LSM COMPOSITE CATHODES

Tad J. Armstrong[*] and Anil V. Virkar[*,z]
Department of Materials Science and Engineering
University of Utah
Salt Lake City, UT 84112

ABSTRACT

Anode-supported cells comprising Ni + yttria-stabilized zirconia (YSZ) anode, thin (~10 μm) YSZ electrolyte, and composite cathodes containing a mixture of $La_{0.8}Sr_{0.2}MnO_{(3-\delta)}$ (LSM) and $La_{0.9}Sr_{0.1}Ga_{0.8}Mg_{0.2}O_{(3-\lambda)}$ (LSGM) were fabricated. The relative proportions of LSGM and LSM were varied between 30 wt.% LSGM + 70 wt.% LSM and 70 wt.% LSGM + 30 wt.% LSM, while the firing temperature was varied between 1000 and 1200°C. The cathode interlayer composition had a profound effect on cathode performance at 800°C with overpotentials ranging between 60 and 425 mV at 1.0 A/cm^2 and exhibiting a minimum for 50 wt.% LSGM + 50 wt.% LSM. The cathodic overpotential decreased with increasing firing temperature of the composite interlayer in the range $1000 \leq T \leq 1150$°C, and then increased dramatically for the interlayer fired at 1200°C. The cell with the optimized cathode interlayer of 50 wt.% LSM + 50 wt.% LSGM fired at 1150°C exhibited an area specific cell resistance of 0.18 Ωcm^2 and a maximum power density of 1.4 W/cm^2 at 800°C. Chemical analysis revealed that LSGM reacts with YSZ above 1000°C to form the pyrochlore phase, $La_2Zr_2O_7$. The formation of the pyrochlore phase at the interface between the LSGM/LSM composite cathode and the YSZ electrolyte limits the firing time and temperature of the cathode interlayer.

[*] Electrochemical Society Active Member
[z] E-mail: anil.virkar@m.cc.utah.edu

I. INTRODUCTION

Anode-supported solid oxide fuel cells (SOFC) are attractive for power generation using fossil fuels since they exhibit low area specific resistance resulting in high power densities at temperatures ≥ 800°C.[1] The state-of-the-art anode-supported SOFC with yittria-stabilized zirconia (YSZ) thin film (10-20 μm) electrolyte exhibit relatively low ohmic contribution of the electrolyte, as compared to electrolyte-supported cells. In addition, the use of anodes fabricated from highly porous cermets, such as Ni/YSZ or Ni/samarium doped ceria (SDC), dramatically reduces the activation and concentration polarizations at the anode.[2-4] Concentration polarization losses at the cathode are usually small as long as the cathode is sufficiently porous, and thin. Also, the ohmic contribution of the cathode is usually small (for anode-supported and electrolyte-supported cells) due to the relatively high electronic conductivity of the cathode. Even so, the performance of anode-supported solid oxide fuel cells operating at temperatures below 800°C is largely limited by the cathode due to large activation overpotentials.[5,6] One approach to improving the performance of the cathode is to use a composite cathode, which typically consists of a two-phase mixture of a solid electrolyte, such as YSZ, and an electrocatalyst, such as, $La_{1-x}Sr_xMnO_{3-\delta}$ (LSM).[7,8] With the use of composite cathodes, the overpotential at the cathode is decreased by spreading out the reaction zone and increasing the three-phase boundary length (TPB).

The performance of a composite cathode depends on: (1) Intrinsic material properties of the electrocatalyst and the solid electrolyte, and (2) Microstructure of the composite cathode, which in turn depends on processing. Intrinsically, the activation polarization of

the composite cathode depends on material properties including the oxide ion conductivity of the solid electrolyte in the cathode and the charge transfer resistance at the three phase boundary between the electrocatalyst, the solid electrolyte in the cathode, and the gas phase.[7,8] In addition, the ohmic resistance of the composite cathode is largely a function of the electronic conductivity of the electrocatalyst. Typically, materials such as LSM or $La_{1-x}Sr_xCoO_{3-\delta}$ (LSC) are used as electrocatalysts, and YSZ or SDC are used as the solid electrolyte. For a composite cathode comprised of a given material system, the microstructure plays an important role in its performance. The activation polarization of the composite cathode is dependent on the three phase boundary length, and thus on the grain size of the solid electrolyte, the particle size of the electrocatalyst, and their relative amounts.[7,8] The concentration polarization is dependent on the porosity of the cathode and thus restriction to gas flow and binary diffusion. In addition, the ohmic resistance of a composite cathode is a function of contiguity of the phases, and the degree of bonding between the cathode and the electrolyte.

The use of composite cathodes consisting of LSM-YSZ and LSC-SDC has been previously reported and the addition of a solid electrolyte (YSZ or SDC) along with the electrocatalyst (LSM or LSC) has been shown to improve the performance of the cathode as compared to the pure electrocatalysts.[9,10] However, deleterious chemical reactions were reported between LSM and YSZ, and LSC and YSZ. For example, LSM and YSZ react to form secondary phases including the pyrochlore $La_2Zr_2O_7$ and the perovskite $SrZrO_3$ at temperatures above 1200°C.[11,12] Even more reactive than LSM is LSC, which reacts with YSZ at temperatures as low as 1000°C to form similar secondary phases.[13]

Although LSC and SDC do not react, a barrier layer between an LSC-SDC composite cathode and YSZ electrolyte is necessary to prevent the formation of secondary phases by reaction of LSC with YSZ.[9,14]

The perovskite oxide ion conductor $LaGaO_3$ doped with Sr and Mg (LSGM) is reported to exhibit superior oxide ion conductivity as compared to YSZ.[15,16] The oxide ion conductivity of LSGM is ~0.1 S/cm at 800°C as compared to ~0.02 S/cm for YSZ. Electrolyte-supported solid oxide fuel cells with LSGM as the solid electrolyte have been reported to exhibit power densities of ~0.7 W/cm^2 at 800°C.[17-19] Furthermore, LSGM and LSM do not react to form resistive secondary phases as is the case with LSM and YSZ, or LSC and YSZ. However, some interdiffusion of La, Sr, Ga, Mg, and Mn is reported to occur between LSGM and LSM, but without the formation of a secondary phase.[20] Thus, the high oxide ion conductivity and phase compatibility with LSM makes LSGM a candidate for use in composite cathodes.

In this study, anode-supported cells were fabricated with composite cathodes consisting of mixtures of LSGM and LSM. The composition and the firing temperature of the composite cathode were varied and the resulting effects on electrochemical performance of the cathode and the cells were studied. In addition, chemical interactions between LSGM and YSZ were studied at various temperatures.

II. EXPERIMENTAL PROCEDURE

The anode-supported solid oxide fuel cells of the present study are comprised of five component layers: a Ni/YSZ composite anode support, a Ni/YSZ anode interlayer, a thin film YSZ electrolyte, an LSGM/LSM composite cathode interlayer, and an LSM current collecting cathode layer. The Ni/YSZ anode is thick relative to the other four layers and provides the support and mechanical integrity to the fuel cell. The anode substrates were prepared by, tape casting a solvent-based slip consisting of 80 wt.% NiO and 20 wt.% YSZ, and an organic pore former. Multiple tapes were laminated together in order to achieve an anode thickness of approximately 1.0 mm. The anodes used in this work were taken from the same batch of tape in order to minimize possible differences in the anode from cell to cell. Circular cells with a diameter of approximately 3 cm were cut from the tape and were subsequently bisqued at 1000°C in air for one hour in order to remove the binders and pore formers and to partially sinter the green part. An anode interlayer of 60 wt.% NiO and 40 wt.% YSZ was deposited on the anode by suspending the powders in a solvent and spraying the mixture on the anode support. The anodes with the anode interlayers were fired a second time at 1000°C for one hour resulting in an anode interlayer of approximately 20 μm in thickness. Similarly, the YSZ electrolyte was deposited by spraying YSZ (TZ-8Y) powder suspended in a solvent onto the bisqued part. The cell was fired at 1400°C for 2 hours resulting in a dense YSZ film with a thickness of ~10 μm.

The composite cathode interlayer was prepared from $La_{0.9}Sr_{0.1}Ga_{0.8}Mg_{0.2}O_{(3-\lambda)}$ (LSGM) and $La_{0.8}Sr_{0.2}MnO_{(3-\delta)}$ (LSM) (Praxair) powders. The relative amounts of LSGM and LSM were varied between 30 and 70 wt.% LSGM and 70 and 30 wt.% LSM. The two powders were mixed with a solvent-binder system in order to form a paste that was subsequently applied to the YSZ electrolyte by a modified screen-printing method. The cells were masked before printing to produce a uniform area of cathode coverage of 1 cm^2 that was fixed for all cells. The composite cathode interlayer was fired at a temperature between 1000 and 1200°C for 2 hours in air. The composite cathode interlayers were between 20 and 25 μm thick after firing. The final LSM cathode current collecting layer was applied in a paste form by a similar method. In addition, a platinum reference electrode was applied on the electrolyte in close proximity to the cathode. The LSM cathode current collector layer was fired at 1000°C for 2 hours and had a thickness of approximately 50 μm after firing. A schematic of the single cells used for testing is shown in Figure 1(a), along with the placement of reference electrodes.

The performance and electrochemical properties of the fuel cells were measured in a spring loaded testing fixture shown in Figure 1(b). The spring-loaded fixture ensures good electrical contact and good sealing, thus preventing leakages. Nickel mesh and silver mesh were used for current collection on the anode and cathode sides, respectively. A high temperature gasket was used for sealing. The cathode side of the cell was exposed to flowing air at a rate of 0.9 l/min. The anode side was exposed to a flowing stream of hydrogen gas saturated with water vapor at 25°C (pH_2O ~ 0.032 atm) at a rate of 0.1 l/min. The NiO/YSZ composite anodes were reduced, *in situ,* at 800°C for 24 h before

electrochemical measurements were conducted at 800°C. During testing, the voltage differences between the anode and the reference electrode, and the cathode and the reference electrode were measured. The ohmic resistance of the cells was measured by current interruption. The DC current was cycled with a potentiostat/galvanostat (EG&G 263A) and the voltages between the cathode, the anode, and the reference electrode were recorded by a digital oscilloscope (Agilent 54662A). The overpotentials were determined by correcting for the requisite ohmic contributions.

In order to investigate the possibility of chemical interactions between LSGM and YSZ, powders of LSGM and YSZ were mixed, milled, and fired at a temperature between 1000 and 1200°C for 2 hours. In addition, to study the possible reaction at the interface between LSGM and YSZ, a thin layer of LSGM was applied on sintered YSZ pellets by a modified screen-printing method and fired at a temperature between 1000 and 1200°C for 2 hours. The samples were then characterized using X-ray powder diffraction (XRD) to identify any secondary phases that may form at the interface. In order to determine the chemical composition of the resulting phases, sintered samples of LSGM and YSZ were prepared. LSGM and YSZ powders were mixed, milled, pelletized, and sintered at temperatures between 1000 and 1200°C. The pellets were polished and evaluated with electron dispersive spectroscopy (EDAX).

III. RESULTS AND DISCUSSION

A scanning electron micrograph (SEM) of a typical anode-supported cell is shown in Figure 2. The micrograph shows the porous LSGM/LSM composite cathode (top), the dense YSZ electrolyte film, and the porous Ni/YSZ anode interlayer (bottom). The composite cathode of this particular cell contained 50 wt.% LSGM and 50 wt.% LSM, which was fired at 1150°C for 2 hours.

The effect of cathode composition on cell performance was studied by varying the relative composition of the composite cathode interlayer between 30 and 70 wt.% LSGM and 70 and 30 wt.% LSM. For this study, the composite cathode interlayers were fired at the same temperature of 1150°C for two hours. The other components of the cells, including the anode, anode interlayer, electrolyte film, and cathode current collecting layer, were fabricated in batch processes under standard conditions in order to minimize differences from cell to cell. SEM analysis confirmed that the composite cathode interlayers partially sintered to form a contiguous two-phase structure while still containing a substantial amount of open porosity necessary for adequate gas flow. In addition, the composite cathode interlayers appeared firmly bonded to the dense YSZ electrolyte and no signs of delamination were observed before or after testing of the cells. The performance curves for cells with composite cathode interlayers of various compositions fired at 1150°C are shown in Figure 3. The cell testing was conducted at 800°C. The maximum power density increased with increasing LSGM content in the composition range 30 to 50 wt.% LSGM and then decreased for LSGM compositions

greater than 50 wt.%. The overall area specific resistance (ASR) of the cell decreased with increasing LSGM content up to 50 wt.% and then increased again for LSGM contents greater than 50 wt.%. The cell with the 50 wt.% LSGM + 50 wt.% LSM composite cathode interlayer exhibited the best performance with a maximum power density of 1.4 W/cm^2 at 2.6 A/cm^2 and an overall cell ASR of 0.18 Ωcm^2.

The overpotentials at the anode and the cathode, as well as the ohmic overpotential (IR drop) of the cells, were measured with a reference electrode located next to the cathode. Calculations of Winkler *et. al.* have shown that that the measured overpotentials depend upon the relative position of the reference electrode.[21] The implied recommendation is that on anode-supported cells, one should not use a reference electrode. However, it is the experience in our laboratory that while some errors in the absolute values of overpotentials measured may well exist, reference electrode is still a valuable tool in evaluating relative differences in electrochemical performance of cells, especially when all other parameters are fixed, and only one parameter is varied. In an attempt to minimize measurement errors and variations from cell to cell, all cells from this work were made from a single anode support tape. In addition, care was taken to ensure that the thickness and the morphology of the anode interlayer, the thickness of the electrolyte layer, the morphology and the thickness of the cathode current collector layer, and the thickness of the cathode interlayer, were essentially the same for all cells. The only variability was in the composition of the cathode interlayer (and any associated morphological differences that arise due to differences in the cathode interlayer composition), or the firing temperature (and any associated morphological changes that

arise due to differences in firing temperatures). In this manner, differences in the measured cathode overpotentials could be attributed to differences in the cathode interlayer.

The anode overpotential as a function of current density for cells with cathode interlayer compositions between 30 and 70 wt.% LSGM and 70 and 30 wt.% LSM are shown in Figure 4. Note that the anode overpotential at 1.0 A/cm^2 varies between ~30 mV and ~50 mV. The total ohmic overpotentials (IR drops) as a function of current density for the same cells are shown in Figure 5. At a current density of 1.0 A/cm^2, the ohmic overpotential varies between ~100 and ~125 mV. The corresponding area specific ohmic resistances of the cells with cathode interlayer compositions of 30/70, 60/40, and 70/30 were approximately 0.125 Ωcm^2, while that for the cells with cathode interlayer compositions of 40/60 and 50/50 were lower with a value of approximately 0.1 Ωcm^2. The total ohmic overpotential (IR drop) measured includes contributions from the anode, electrolyte, and cathode. The estimated ohmic resistance of a 10 μm YSZ electrolyte layer is 0.05 Ωcm^2 at 800°C. Thus, over half of the ohmic resistance of the cell is due to the anode and the cathode. Furthermore, since the anodes were prepared from the same tape, the higher ohmic resistances of the cells with cathode interlayer compositions of 30/70, 60/40, and 70/30 as compared to the cells with cathode interlayer compositions of 40/60 and 50/50 must be due to differences in the cathode interlayer. Because of the higher electronic conductivity of LSM as compared to YSZ, it is expected that the ohmic resistances of the cathode interlayers would decrease with increasing LSM content. The lower ohmic resistances of the cells with cathode interlayers containing 50 and 60 wt.%

LSM as compared to those with only 30 and 40 wt.% LSM is consistent with this notion. However, the high ohmic resistance of the cell with LSM rich 30/70 cathode interlayer indicates that other factors, such as sinterability and bonding between cathode interlayer and electrolyte, are likely factors, which determine the ohmic resistance.

The overpotentials at the cathode as a function of current density are shown in Figure 6. As seen in the figure, the cathode interlayer composition has a profound effect on the overpotential at the cathode with the worst performing cell (70/30) exhibiting an overpotential of approximately 425 mV at 1.0 A/cm^2 while the best performing cell (50/50) with an overpotential of only 60 mV at 1.0 A/cm^2, which is a difference of 365 mV. Note that this difference is much greater than even the absolute values of anodic and ohmic overpotentials. As the differences in the anodic overpotentials and ohmic overpotentials were less than 25 mV, it is clear that errors due to surface mounting of a reference electrode must be small (for < 1 A/cm^2). For this reason, it can be concluded that measurements made with respect to a reference electrode are valuable in assessing the performance of the cathode.

Since the cathode interlayers are comprised of the same materials, LSGM and LSM, the differences in performance with variation in relative amounts of LSGM and LSM are likely due to microstructural and compositional differences. Firstly, in order for composite electrodes to be effective, the two phases must be contiguous throughout the electrode. Typically a minimum of 30 vol.% of a phase must be present to ensure contiguity, with this value being higher depending on the amount and the morphology of

porosity. The theoretical densities of LSGM and LSM are approximately 6.2 g/cm^3 and 6.5 g/cm^3, respectively. Thus, approximate volume % of the two phases must be in proportion to their wt.%. Therefore, for the 30/70 and 70/30 cathode interlayer compositions, it is possible that one of the two phases has low contiguity in the electrode. In cases where the two phases are indeed contiguous, it has been shown that the performance of composite electrodes is dependent on porosity and three-phase boundary length (TPB). The porosity in the electrode must be adequate to allow for the transport of gases in and out of the electrode. In cases where the porosity is low and/or the current densities are high, the effects of concentration polarization can be large and may adversely affect the performance of a cell. SEM analysis, however, shows that the LSGM/LSM composite cathodes (Figure 2) are highly porous. Although some differences in porosity may occur with differing compositions of the composite cathode interlayer, the effects of concentration polarization are small at low current densities. Thus, the large differences in cathode overpotentials at current densities below 0.5 A/cm^2 (Figure 6) are likely due to changes in the three phase boundary length (TPB) and thus dominated by activation polarization. The effects of TPB on the activation polarization of composite electrodes have been analyzed by several groups including Kenjo *et. al.* and Tanner *et. al.* [7,8] In the model proposed by Tanner et. al., the effective charge transfer resistance (R_{ct}^{eff}) depends on the intrinsic charge transfer resistance (R_{ct}) and the electrode microstructure such that

$$R_{ct}^{eff} = \sqrt{\frac{R_{ct} d \rho_i}{(1 - V_V)}} \qquad [1]$$

where, ρ_i is the ionic resistivity of the solid electrolyte (LSGM) in the cathode, V_V is the volume percent of porosity, and d is a microstructural parameter related to the particle

size of solid electrolyte in the cathode. The intrinsic charge transfer resistance (R_{ct}) is given as

$$R_{ct} = \frac{\rho_{ct}}{l_{TPB}} \quad [2]$$

where ρ_{ct} is the charge transfer resistivity and l_{TPB} is the three phase boundary length. The ionic resistivity ρ_i, a property of solid electrolyte part of the composite cathode, and the charge transfer resistivity ρ_{ct}, a property of the electrocatalyst, solid electrolyte, and gas phase system, are dependent on material properties. The volume percent of porosity V_V**,** particle size d, and three-phase boundary length l_{TPB}, by contrast, are microstructural parameters. The effective charge transfer resistance can be rewritten as

$$R_{ct}^{eff} = \sqrt{\rho_{ct}\rho_i}\sqrt{\frac{d}{l_{TPB}(1-V_V)}} \quad [3]$$

in order to separate and emphasize the effects of the fundamental material properties from the microstructural properties. For the LSGM/LSM composite cathodes studied, the ionic resistivity of LSGM and the intrinsic charge transfer resistivity of the LSGM/LSM system are constant and should not vary from cell to cell[1]. Furthermore, the different compositions of composite cathodes were prepared from the same starting LSGM and LSM powders. For a given firing temperature, the particle size of the electrolyte d should not vary to a large degree, since the maximum cathode firing temperature was only 1200^{o}C, while the typical sintering temperature of LSGM is above 1500^{o}C. Thus, changes in the effective charge transfer resistance for various compositions of composite cathode should primarily be due to varying TPB length. At low current densities, the charge transfer resistance of the cathode can be estimated from the linear portions of the

[1] This is strictly not true, as the ionic conductivity of LSGM is expected to be a function of the grain size.

overpotential versus current density plots. Also, the effective exchange current density can be determined using the low current density approximation of the Butler-Volmer equation, since it is inversely proportional to the effective charge transfer resistance, R_{ct}^{eff}. The area specific charge transfer resistance and the exchange current density for composite cathodes of various compositions are given in Table I. The area specific charge transfer resistance varies from 0.557 Ωcm^2 for the cathode of 30/70 composition to 0.242 Ωcm^2 for the cathode of 50/50 composition. The cell with the 50/50 cathode interlayer exhibited the lowest charge transfer resistance, which is consistent with its low cathode overpotential (Figure 6) and a high power density (Figure 3). The anodic and the cathodic overpotentials, and the total ohmic overpotential (IR drop) for the cell with the 50/50 cathode interlayer fired at 1150°C are shown in Figure 7. For this cell, the anodic and cathodic overpotential contributions to the total overpotential losses are simliar and lower than that due to the total ohmic resistance.

In addition to the cathode interlayer composition, the firing temperature of the cathode interlayer was varied and the resulting effects on cell performance were investigated. The cathode interlayer composition was fixed at 50 wt.% LSGM and 50 wt.% LSM, and fired at a temperature between 1000 and 1200°C for two hours. The voltage and the power density curves as a function of current density for these cells measured at 800°C are shown in Figure 8. The total area specific resistance decreases from 0.20 Ωcm^2 to 0.16 Ωcm^2 with increasing firing temperature from 1000°C to 1150°C, but then increases dramatically to 0.24 Ωcm^2 for a firing temperature of 1200°C. Thus, as expected, the power density increases from approximately 1.0 W/cm^2 to 1.4 W/cm^2 with an increasing

firing temperature between 1000 to 1150°C, and then decreases to ~0.6 W/cm^2 for the interlayer fired at 1200°C. The anode overpotential, as a function of current density for the cells tested at 800°C, is shown in Figure 9. Similar to the cells previously tested (Figure 4), the anode overpotential at 1.0 A/cm^2 varies over a range of about 20 mV. The ohmic overpotentials (IR drop) of the cells as a function of current density are shown in Figure 10. The ohmic resistances for the cells with cathode interlayers fired at 1000, 1050, and 1100°C are approximately the same with a value of 0.125 Ωcm^2. The ohmic resistance of the cell whose cathode interlayer was fired at 1150°C is lower with a value of 0.1 Ωcm^2, while that for the interlayer fired at 1200°C is higher with a value of approximately 0.175 Ωcm^2. The lower area specific resistance of the sample with cathode interlayer fired at 1150°C may be due do to better bonding between the cathode to the electrolyte thus reducing the contact resistance at the interface. The high resistance of the cell with the cathode interlayer fired at 1200°C may be due to the formation of an intermediate phase at the interface between the cathode and the electrolyte. This possibility will be discussed later.

The cathode overpotentials as function of current density for the cells with 50/50 interlayers fired at temperatures between 1000 and 1200°C are shown in Figure 11. The overpotential at the cathode decreases with increasing firing temperature in the range 1000 to 1150°C, then dramatically increases for the interlayer fired at 1200°C. At 1.0 A/cm^2, the cathode overpotential varies between a low of 65 mV for the interlayer fired at 1150°C to a high of 250 mV for the interlayer fired at 1200^{o}C. The effective charge transfer resistances and the effective exchange current densities for cathodes with

interlayers fired at various temperatures are summarized in Table II. The effective charge transfer resistance decreases with increasing firing temperature in the range 1000 to 1150°C, and then increases again above 1150°C. The decrease in charge transfer resistance at the cathode with increasing firing temperature of the interlayer (1000°C ≤ T ≤ 1150°C) is likely due to more complete sintering (better particle-to-particle contact). The effective charge transfer resistance is dependent on particle size *d*, three-phase boundary length l_{TPB}, and volume percent porosity V_V as modeled by equation 3. At higher firing temperatures (1200°C), it is possible that either a reaction between the electrocatalyst and the ionic conductor occurs wherein the intrinsic charge transfer resistivity is adversely affected, or that the microstructure is adversely affected, or both. Unless detailed microstructural analysis is conducted, it would be difficult to decipher the exact reason(s).

An examination of Figures 6 and 11 shows that cathodic overpotential exhibits a complex dependence on current density. Specifically, it is seen that in many cases, over some current density range, the overpotential is almost independent of current density ($d\eta_{cathode} / di \approx 0$). It is not known if this is a real effect, or a possible artifact of uncertainties related to the placement of reference electrodes.

In order to determine whether chemical reactions at the cathode played a role in the poor performance of the cell whose cathode was fired at 1200°C, possible chemical interactions between LSGM and LSM and LSGM and YSZ were investigated. Chemical interactions between LSM and YSZ at elevated temperatures have been reported.[11,12]

LSM and YSZ react to form the secondary phase $La_2Zr_2O_7$ at temperatures above 1200°C. In the present study, the phase $La_2Zr_2O_7$ was not detected by XRD in milled mixtures of LSM and YSZ powder fired at temperatures between 1000 and 1200°C for two hours. Since the maximum cathode firing temperature was 1200°C, it may be concluded that reaction between LSM and YSZ is not responsible for the poor performance of the cathode fired at 1200°C. Similarly, no secondary phases were detected by XRD for milled mixtures of LSGM and LSM powder fired for two hours at a temperature as high as 1200°C. This is in agreement with previous work by Huang *et. al.* which reported inter-diffusion of La, Sr, Mn, and Ga between LSM and LSGM with no phase transformations.[20] Possible reactions between LSGM and YSZ were investigated by milling and firing mixtures of LSGM and YSZ powders at temperatures between 1000 and 1200°C for two hours. X-ray powder diffraction patterns of the powders after firing are shown in Figure 12. In the temperature range 1000 to 1200°C, LSGM reacts with YSZ to form a secondary phase with a cubic crystal structure, which was indexed as the pyrochlore $La_2Zr_2O_7$ (JCPDS 17-0450). The relative amount of the pyrochlore phase increases with increasing temperature in the range, $1000 \leq T \leq 1200$°C. For the powder mixture fired at 1200°C for two hours, no LSGM was detectable by XRD and appears to have completely reacted with YSZ. Other than the pyrochlore, no other phases were found in any of the patterns. In order to determine if Ga dissolved into $La_2Zr_2O_7$ or YSZ, energy dispersive spectroscopic (EDS) analysis was performed on dense samples fabricated from LSGM and YSZ powders fired at 1000, 1100, and 1200°C. The presence of Ga was detected in the pyrochlore phase but not in YSZ. This shows that LSGM reacts with YSZ to form Ga doped cubic $La_2Zr_2O_7$. It was not determined whether Ga

substitutes on La or Zr sites of the $La_2Zr_2O_7$ pyrochlore phase. The six coordinated Ga^{3+} ion is closer in size to the Zr^{4+} ion than the larger La^{3+} ion[22]. Thus, it is the expectation that Ga^{3+} ion may substitute for the Zr^{4+} ion resulting in an oxygen deficient pyrochlore, $La_2Zr_{2-x}Ga_xO_{7-\delta}$.

In all fuel cells tested, a mixture of LSGM and LSM powder was screen-printed onto an already sintered dense layer of YSZ. In order to investigate a possible reaction at this interface, LSGM powder in the form of a paste was screen-printed onto dense YSZ pellets and then fired at 1000, 1100, and 1200°C for two hours. After firing, the LSGM side of the pellets was analyzed with XRD and the samples were sectioned and analyzed with EDS. The presence of a pyrochlore phase was not detected with XRD indicating that the reaction was limited to the interface. EDS analysis of the cross section of the cell, whose cathode was fired at 1200°C, revealed a thin reaction layer of approximately 4 μm in thickness between the LSGM and YSZ regions. The thickness of the reaction zone for the sample fired at 1100°C was less than 0.5 μm, while that for the 1000°C sample was not detectable. The formation of a thin layer of the resistive, Ga-containing $La_2Zr_2O_7$ pyrochlore phase between the cathode interlayer and YSZ electrolyte, when fired at 1200°C for two hours, appears to increase the ohmic resistance of the cell and the cathodic overpotential and is thus detrimental to the performance of the cell.

IV. CONCLUSIONS

Anode-supported solid oxide fuel cells were fabricated with a thin film YSZ electrolyte and a composite cathode, consisting of a mixture of $La_{0.9}Sr_{0.1}Ga_{0.8}Mg_{0.2}O_{(3-\lambda)}$ (LSGM) and $La_{0.8}Sr_{0.2}MnO_{(3-\delta)}$ (LSM). The relative compositions and firing temperatures of the composite cathode interlayers were varied and the resulting effects on cell performance were investigated. Variations in the composition of the cathode interlayer had a profound effect on the overpotential at the cathode and the performance of the cells. In the composition range 30 to 70 wt.% LSGM and 70 to 30 wt.% LSM, the cathodic overpotential varied between 65 mV and 400 mV at 1.0 A/cm^2 at 800°C and exhibited a minimum for the 50/50 composition. The large change in cathodic performance with composition is reflected in the maximum power densities of the cells, which varied between 0.4 and 1.4 W/cm^2. In addition to compositional changes, the cathode interlayer firing temperature was varied between 1000 and 1200°C while the composition was fixed at 50 wt.% LSGM + 50 wt.% LSM. The overpotentials at the cathode decreased with increasing firing temperature in the range $1000 \leq T \leq 1150$°C, and then increased again for the interlayer fired at 1200°C. The effects of cathode interlayer firing temperature on cell performance are dramatic, with maximum power densities ranging between 0.6 and 1.4 W/cm^2 for firing temperatures of $1000 \leq T \leq 1200$°C. The dramatic decrease in performance between the cell with the cathode interlayer fired at 1150°C and the one fired at 1200°C is attributed to a phase reaction between LSGM and YSZ. Chemical analysis and powder X-ray diffraction revealed that LSGM reacts with YSZ above 1000^{o}C to form the pyrochlore phase $La_2Zr_2O_7$. The formation of this resistive pyrochlore phase at the interface between the LSGM/LSM composite cathode and the YSZ

electrolyte may limit the firing time and temperature of the cathode interlayer. The cathode interlayer was optimized with a composition of 50 wt.% LSGM and 50 wt.% LSM and a firing temperature of 1150°C, resulting in a cell exhibiting an area specific resistance of 0.18 Ωcm^2 and a maximum power density of 1.4 W/cm^2 at 800°C.

Acknowledgements: This work was supported by the U. S. Department of Energy, NETL, under Contract No. DE-AC26-99FT40713.

REFERENCES

1. J-W. Kim, A. V. Virkar, K. Z. Fung, K. Mehta, and S. C. Singhal, J. Electrochem. Soc., **146**, 69 (1999).

2. C. Wen, R. Kato, H. Fukunaga, H. Ishitani, and K. Yamada,J. Electrochem. Soc., **147**, 2076 (2000).

3. N. Minh, J. Am. Ceram. Soc., **76**, 563 (1993).

4. R. Maric, S. Ohara, T. Fukui, T. Inagaki, and J. Fujita, Electrochem. Solid-State Lett., **1**, 201 (1998).

5. Y. Takeda, R. Kanno, M. Noda, Y. Tomida, and O. Yamamoto, J. Electrochem. Soc., **134**, 2656 (1987).

6. T. Tsai, S. A. Barnett, Solid State Ionics, **98**, 191 (1997).

7. T. Kenjo, S. Osawa, and K. Fujikawa, J. Electrochem. Soc., **138**, 349 (1991).

8. C. W. Tanner, K. Z. Fung, and A. V. Virkar, J. Electrochem. Soc., **144**, 21 (1997).

9. S. Desouza, S. J. Visco, and L. C. DeJonghe, Solid State Ionics, **98**, 57 (1997).

10. M. J. Jorgensen, S. Primdahl, C. Bagger, and M. Mogensen, Solid State Ionics, **139**, 1 (2001).

11. K. Kleveland, M. Einarsrud, C. R. Schmidt, S. Shamsili, S. Faaland, K. Wiik, and T. Grande, J. Am. Ceram. Soc., **82**, 729 (1999).

12. K. Kleveland, M. Einarsrud, C. R. Schmidt, S. Shamsili, S. Faaland, K. Wiik, and T. Grande, J. Am. Ceram. Soc., **82**, 721 (1999).

13. F. M. Figueiredo, J. A. Labrincha, J. R. Frade, and F. M. B. Marques, Solid State Ionics, **101**, 343 (1997).

14. H. Uchida, S. Arisaka, and M. Watanabe, Electrochem. Solid-State Lett., **2**, 428 (1999).

15. M. Feng and J. B. Goodenough, Eur. J. Solid State Inorg. Chem., **31**, 663 (1994).

16. T. Ishihara, H. Matruda, and Y. Takita, J. Am. Chem. Soc., **116**, 3801 (1994).

17. K. Huang and J. B. Goodenough, J. Alloys Cmpd., **303**, 454 (2000).

18. K. Huang, R. Tichy, and J. B. Goodenough, J. Am. Ceram. Soc., **81**, 2581 (1998).

19. T. Ishihara, T. Shibayama, M. Honda, H. Nishiguchi, and Y. Takita, Chem. Commum., **13**, 1227 (1999).

20. K. Huang, M. Feng, J. B. Goodenough, and M. Schmerling, J. Electrochem. Soc., **143**, 2630 (1996).

21. J. Winkler, P. V. Hendriksen, N. Bonanos, and M. Mogensen, J. Electrochem. Soc., **145**, 1184 (1998).

22. R. D. Shannon, *Acta Crystallographica*, **A32**, 751 (1976).

Figure Captions

Figure 1(a). Schematic of a single cell.

Figure 1(b). A schematic of the test fixture for testing of single cells.

Figure 2. A scanning electron micrograph of a fractured single cell.

Figure 3. Voltage and power density as a function of current density for cells with varying cathode interlayer compositions. The cells were tested at 800°C with air and humidified hydrogen.

Figure 4. Anode overpotential as a function of current density for cells with varying cathode interlayer compositions. The cells were tested at 800°C with air and humidified hydrogen.

Figure 5. Ohmic overpotential (IR drop) as a function of current density for cells with varying cathode interlayer compositions. The cells were tested at 800°C with air and humidified hydrogen.

Figure 6. Cathode overpotential as a function of current density for cells with varying cathode interlayer compositions. The cells were tested at 800°C with air and humidified hydrogen.

Figure 7. Anodic, cathodic, and ohmic overpotentials at 800^{o}C for the cell with the 50 wt.% LSGM and 50 wt.% LSM composite cathode fired at 1150°C.

Figure 8. The effect of cathode interlayer firing temperature on performance at 800^{o}C as shown with voltage and power density as a function of current density. The cathode interlayer consisted of 50 wt.% LSGM and 50 wt.% LSM.

Figure 9. Anode overpotential as a function of current density at 800^{o}C for cells with a 50 wt% LSGM and 50 wt% LSM composite cathode fired at various temperatures.

Figure 10. Ohmic overpotential (IR drop) as a function of current density for cells with 50 wt.% LSGM and 50 wt.% LSM composite cathodes fired at various temperatures.

Figure 11. Cathode overpotential as a function of current density for cells with 50 wt.% LSGM and 50 wt.% LSM composite cathodes fired at various temperatures.

Figure 12. Powder X-ray diffraction patterns for LSGM and YSZ powders mixed and fired at temperatures between 1000 and 1200°C for two hours.

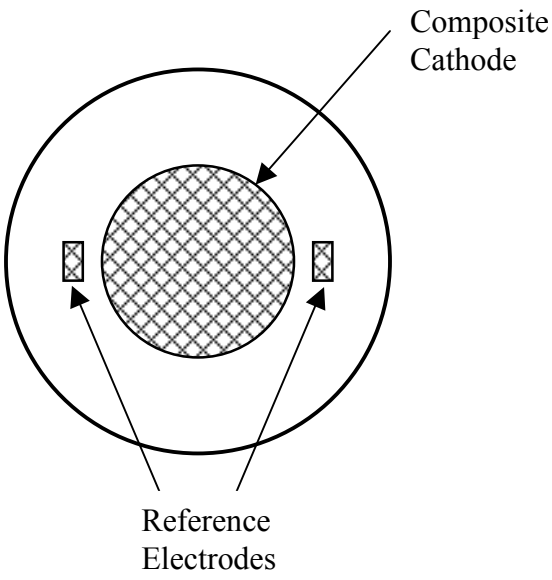

Figure 1(a)

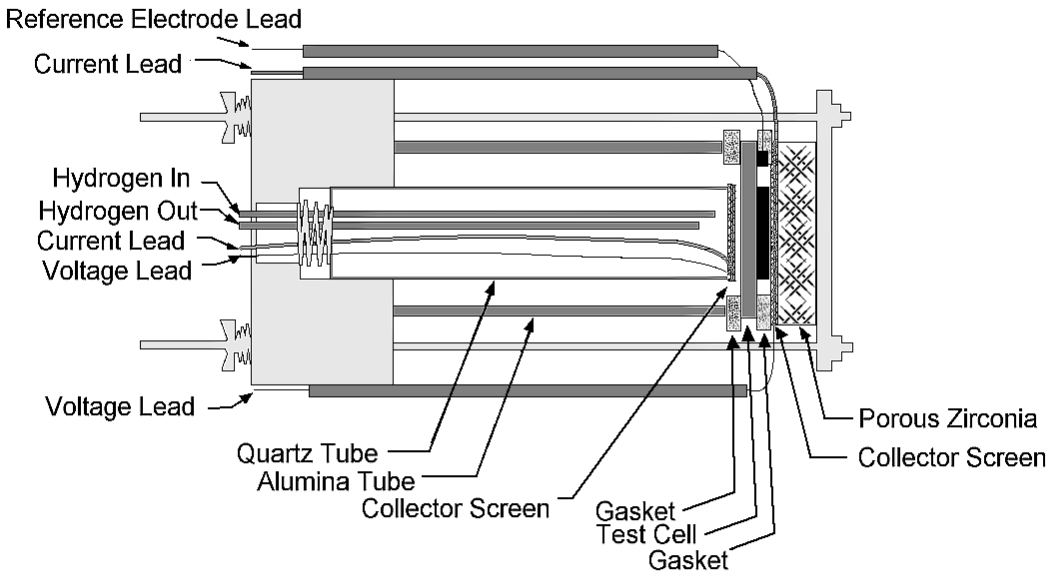
Reference Electrode Lead
Current Lead
Hydrogen In
Hydrogen Out
Current Lead
Voltage Lead
Voltage Lead
Quartz Tube
Alumina Tube
Collector Screen
Gasket
Test Cell
Gasket
Porous Zirconia
Collector Screen

Figure 1(b)

Figure 2

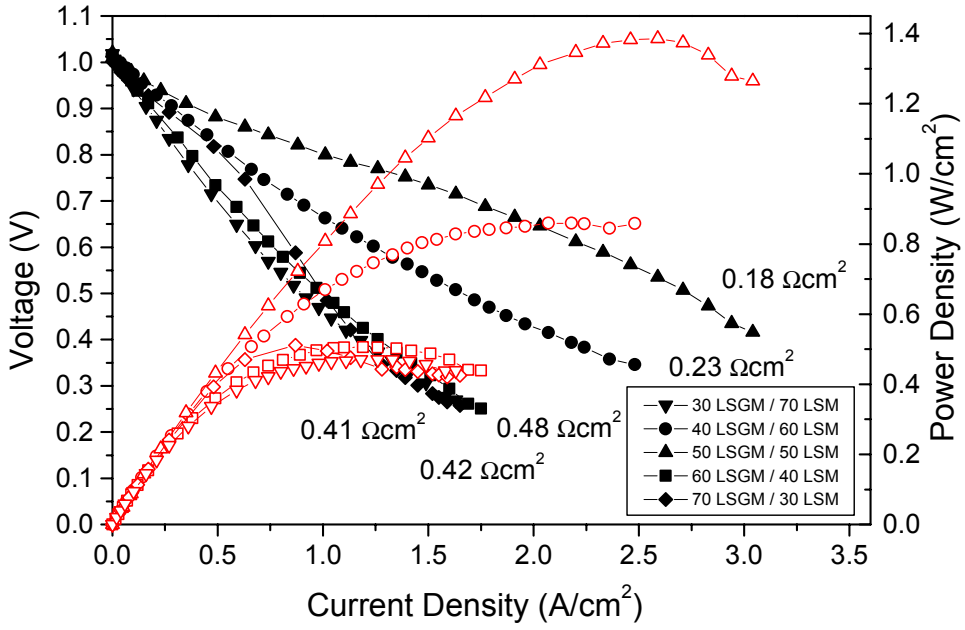
Voltage (V)
Power Density (W/cm^2)
Current Density (A/cm^2)
0.18 Ωcm^2
0.23 Ωcm^2
0.41 Ωcm^2
0.48 Ωcm^2
0.42 Ωcm^2
30 LSGM / 70 LSM
40 LSGM / 60 LSM
50 LSGM / 50 LSM
60 LSGM / 40 LSM
70 LSGM / 30 LSM

Figure 3

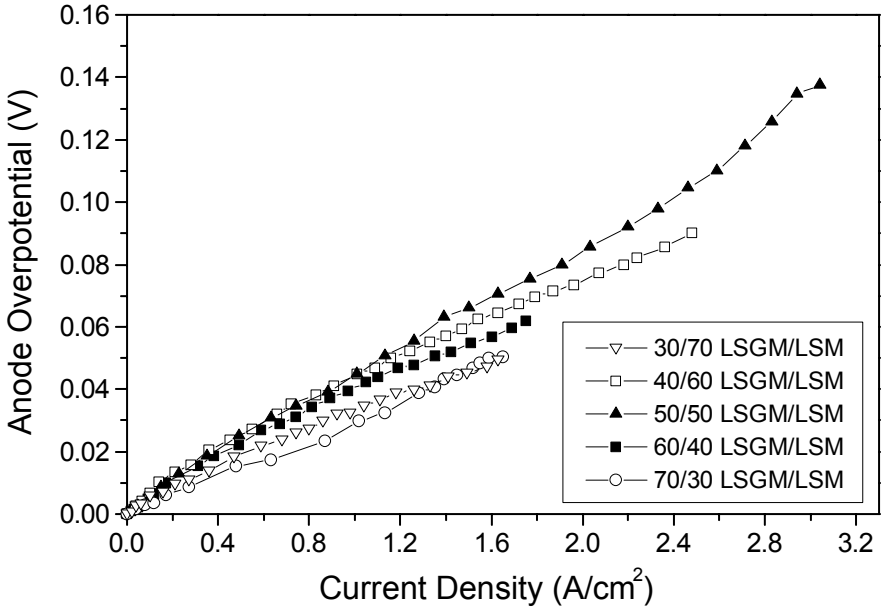
Anode Overpotential (V)
Current Density (A/cm^2)
0.00
0.02
0.04
0.06
0.08
0.10
0.12
0.14
0.16
0.0
0.4
0.8
1.2
1.6
2.0
2.4
2.8
3.2
30/70 LSGM/LSM
40/60 LSGM/LSM
50/50 LSGM/LSM
60/40 LSGM/LSM
70/30 LSGM/LSM

Figure 4

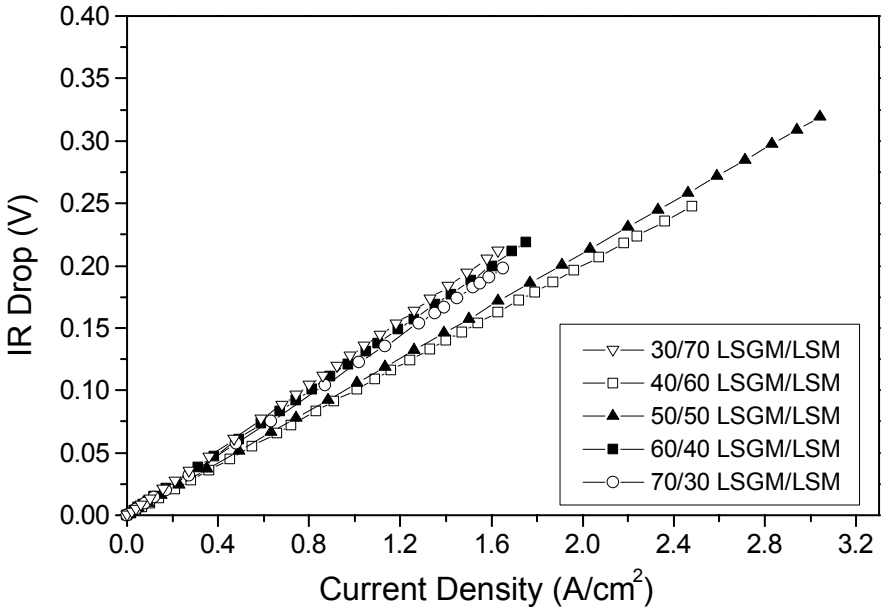
IR Drop (V)
Current Density (A/cm^2)
0.00
0.05
0.10
0.15
0.20
0.25
0.30
0.35
0.40
0.0
0.4
0.8
1.2
1.6
2.0
2.4
2.8
3.2
30/70 LSGM/LSM
40/60 LSGM/LSM
50/50 LSGM/LSM
60/40 LSGM/LSM
70/30 LSGM/LSM

Figure 5

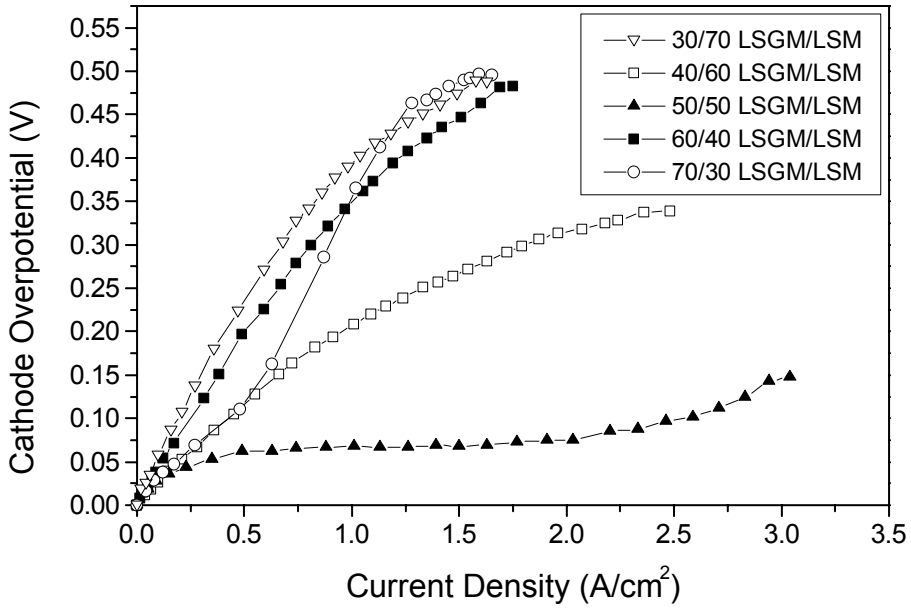
Cathode Overpotential (V)
Current Density (A/cm^2)
0.00
0.05
0.10
0.15
0.20
0.25
0.30
0.35
0.40
0.45
0.50
0.55
0.0
0.5
1.0
1.5
2.0
2.5
3.0
3.5
30/70 LSGM/LSM
40/60 LSGM/LSM
50/50 LSGM/LSM
60/40 LSGM/LSM
70/30 LSGM/LSM

Figure 6

Table I. Charge transfer resistance and exchange current density for composite cathodes with various compositions fired at 1150 °C.

Cathode Composition	30% LSGM 70% LSM	40% LSGM 60% LSM	50% LSGM 50% LSM	60% LSGM 40% LSM	70% LSGM 30% LSM
Charge transfer resistance (Ωcm^2)	0.557	0.277	0.242	0.431	0.417
i_o exchange current density (mA/cm^2)	41.5	83.4	95.4	53.6	55.4

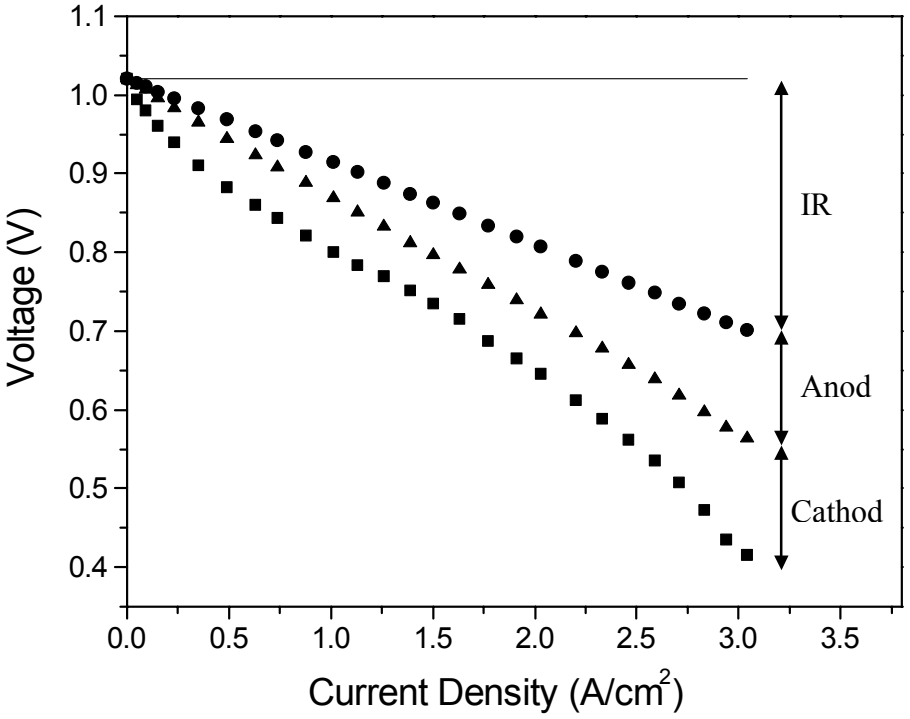
1.1
1.0
0.9
0.8
0.7
0.6
0.5
0.4
Voltage (V)
0.0
0.5
1.0
1.5
2.0
2.5
3.0
3.5
Current Density (A/cm2)
IR
Anod
Cathod

Figure 7

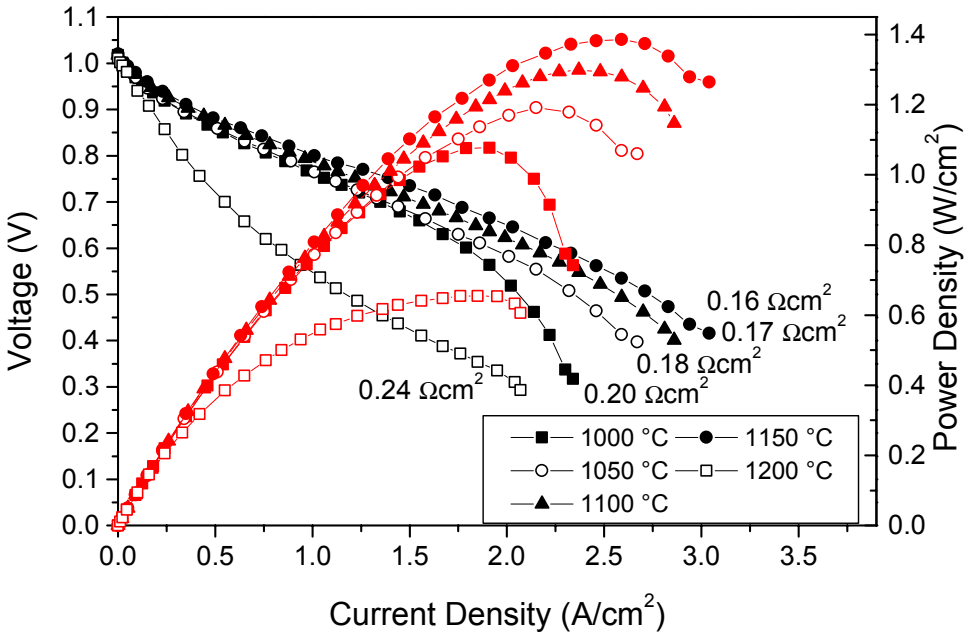
Voltage (V)
Power Density (W/cm^2)
Current Density (A/cm^2)
0.16 Ωcm^2
0.17 Ωcm^2
0.18 Ωcm^2
0.20 Ωcm^2
0.24 Ωcm^2
1000 °C
1150 °C
1050 °C
1200 °C
1100 °C

Figure 8

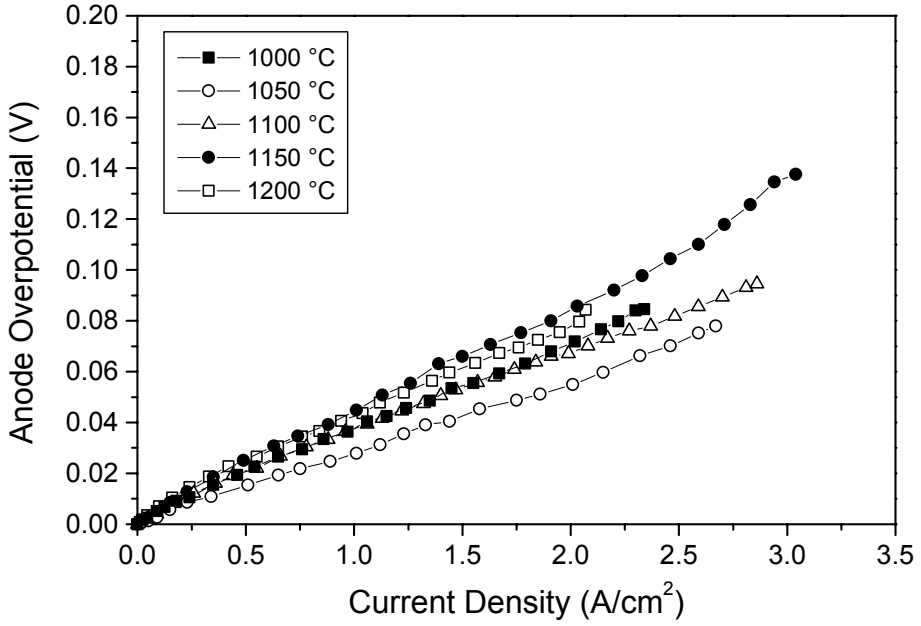
Anode Overpotential (V)
Current Density (A/cm^2)
1000 °C
1050 °C
1100 °C
1150 °C
1200 °C
0.00
0.02
0.04
0.06
0.08
0.10
0.12
0.14
0.16
0.18
0.20
0.0
0.5
1.0
1.5
2.0
2.5
3.0
3.5

Figure 9

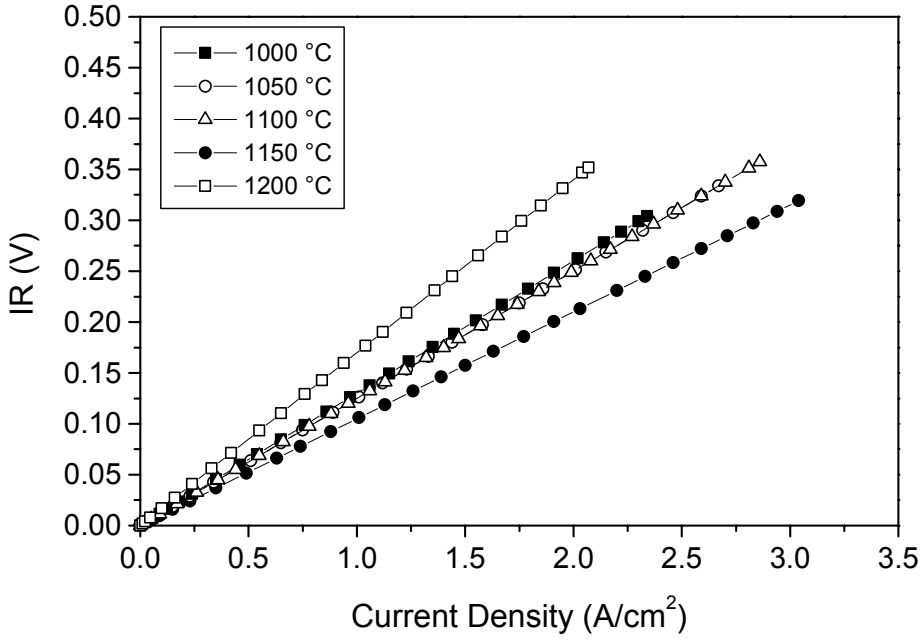

Figure 10

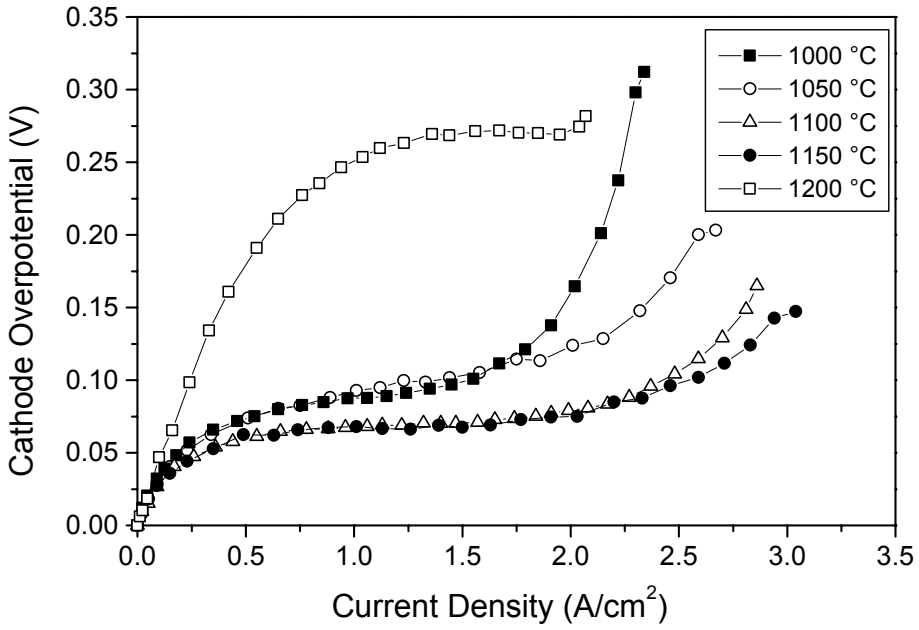
Cathode Overpotential (V)
Current Density (A/cm^2)
0.00
0.05
0.10
0.15
0.20
0.25
0.30
0.35
0.0
0.5
1.0
1.5
2.0
2.5
3.0
3.5
1000 °C
1050 °C
1100 °C
1150 °C
1200 °C

Figure 11

Table II. Charge transfer resistance and exchange current density for the 50 wt% LSGM/50 wt% LSM composite cathode fired at various temperatures.

Cathode Firing Temperature	1000 °C	1050 °C	1100 °C	1150 °C	1200 °C
Charge transfer resistance (Ωcm^2)	0.348	0.323	0.282	0.242	0.405
i_o exchange current density (mA/cm^2)	66.4	71.5	81.9	95.4	57.0

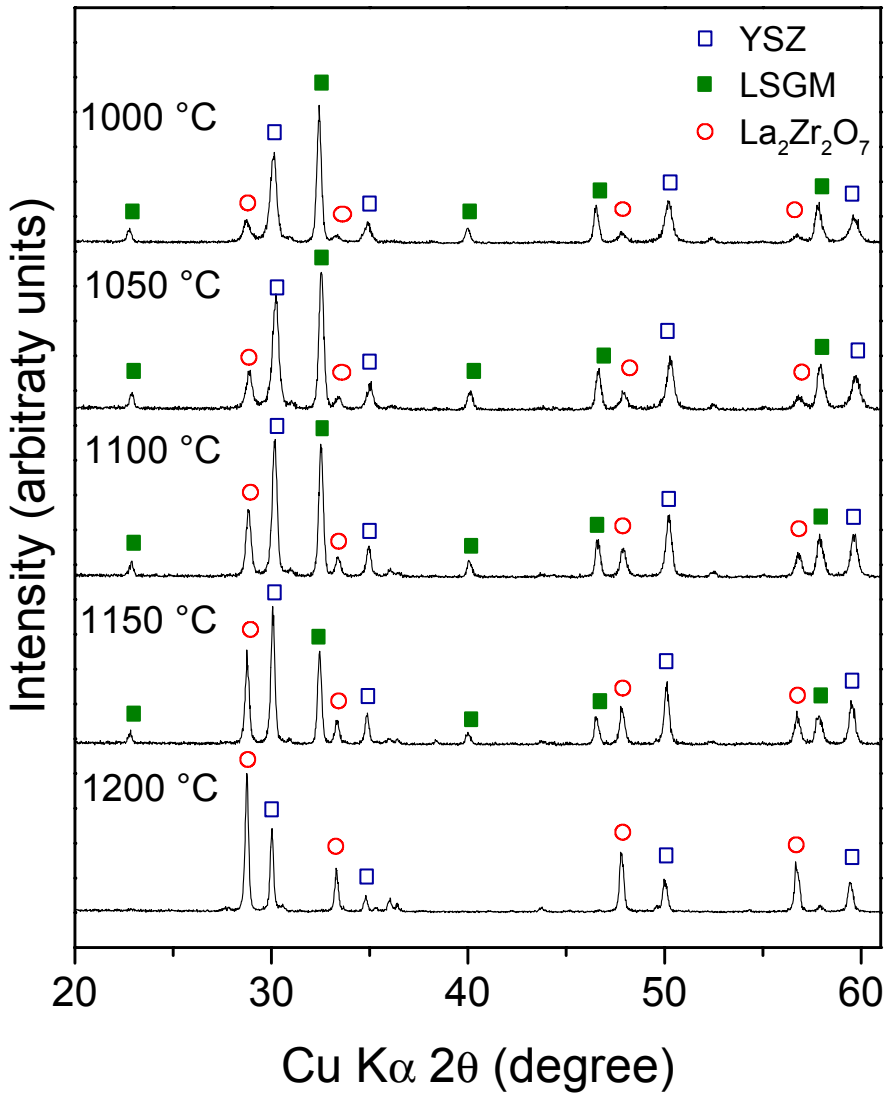
YSZ
LSGM
La2Zr2O7
1000 °C
1050 °C
1100 °C
1150 °C
1200 °C
Intensity (arbitraty units)
20
30
40
50
60
Cu Kα 2θ (degree)

Figure 12

MEASUREMENT OF O_2-N_2 EFFECTIVE DIFFUSIVITY IN POROUS MEDIA AT HIGH TEMPERATURES USING AN ELECTROCHEMICAL CELL

Feng Zhao, Tad J. Armstrong and Anil V. Virkar
Department of Materials Science and Engineering
122 S. Central Campus Drive, University of Utah, Salt Lake City, Utah 84112

ABSTRACT

The effective diffusivity of O_2-N_2 in porous media was measured at high temperatures (650-800°C) using an electrochemical concentration cell. Porous membranes having total porosity between 29 and 48 vol.% were fabricated from Sr-doped $LaMnO_3$ (LSM) with 20 to 30 wt.% carbon added as a pore former. The O_2-N_2 effective binary diffusivity, $D^{eff}_{O_2-N_2}$, at 800°C increased from ~0.016 to ~0.12 cm^2/s with increasing open porosity between 15 and 44 vol.%. The $D^{eff}_{O_2-N_2}$ exhibited a nonlinear dependence on open porosity and increased dramatically for samples with greater than 35 vol.% open porosity. The estimated effective Knudsen diffusivities of O_2 and N_2, $D^{eff}_{O_2K}$ and $D^{eff}_{N_2K}$, at 800°C were an order of magnitude higher than the effective binary diffusivity, $D^{eff}_{O_2-N_2}$. Thus, O_2-N_2 transport through the porous membranes was governed by the effective binary diffusivity, $D^{eff}_{O_2-N_2}$. The effects of O_2-N_2 effective binary diffusivity, $D^{eff}_{O_2-N_2}$, on concentration polarization of cathodes for solid oxide fuel cells were assessed. The nonlinear behavior of the O_2-N_2 effective diffusivity as a function of open porosity indicates that a critical amount of porosity in the cathode is necessary to ensure that the overpotential due to

concentration polarization is small. The temperature dependence of $D^{eff}_{O_2-N_2}$ was investigated between 650 and 800^{o}C, which was found to be in accord with the Chapman-Enskog model.

I. INTRODUCTION

The contribution of concentration polarization to the total polarization at both the anode and cathode of solid oxide fuel cells (SOFC) can be substantial [1,2]. The effects of concentration polarization are most pronounced in electrodes of low porosity and at high current densities. In electrode-supported SOFC, the contribution of ohmic polarization (IR drop) of a thin electrolyte to the total overpotential of the cell is small as compared to that of an electrolyte-supported SOFC. In fact, anode-supported SOFC have been reported wherein the contribution of the electrolyte ohmic polarization (IR drop) is less than that of the combined polarization losses at the two electrodes. Thus, in the case of electrode-supported SOFC, the maximum current density attainable is largely limited by polarization losses at the electrodes. In electrode-supported SOFC, one of the two electrodes, either anode or cathode, is fabricated of a thickness large enough to function as a support and thereby lend mechanical integrity. However, this does not mean that concentration polarization of the support electrode is necessarily greater than that of the thin electrode. For example, anode-supported SOFC are routinely fabricated with anodes consisting of NiO and YSZ composites that are subsequently reduced in-situ resulting in highly porous Ni and YSZ cermets. Measurements conducted on anode-supported SOFC show that overpotential at the thick anode can often be less than that at the thin cathode. Typically, cathodes are fabricated from an electrocatalyst such as Sr-doped $LaMnO_3$ or Sr-doped $LaCoO_3$. In order to generate some porosity, a pore former is typically added and the cathode is fired at temperatures high enough to partially sinter the electrocatalyst, without in the process reducing porosity. However, the amount of porosity necessary to ensure that the concentration polarization is sufficiently small in a cathode at operating temperatures is not very well understood.

Concentration polarization at the cathode is related to the resistance to transport of oxygen gas to the physically distinct cathode/electrolyte interface. Concentration polarization at a given current density depends upon the partial pressure of oxygen in the oxidant, cathode porosity, pore size, and thickness. The cathode-limited current density arises when the partial pressure of oxygen at the cathode/electrolyte interface is nearly zero. For values of current density lower than the limiting current density, the partial pressure of oxygen at the cathode/electrolyte interface is finite (greater than zero). Under such conditions, the current density is proportional to the difference in partial pressures of oxygen in the cathode chamber (outside the cathode), and that at the cathode/electrolyte interface; with the proportionality constant which includes the effective binary diffusivity of O_2-N_2, $D^{eff}_{O_2-N_2}$.

Substantial concentration polarization may well arise from the cathode. Thus, it is desirable to measure the effective O_2-N_2 diffusivity in porous media at high temperatures. A considerable amount of work in the field of experimental and theoretical treatments of the effective diffusivity in porous media has been reported in the open literature [3,4]. Gas transport in porous media is complex and includes contributions from bulk, Knudsen[2], and surface diffusion, as well as viscous flow. The analysis of gas flow is further complicated by interactions with pore structure, for example adsorption/desorption processes on the internal surfaces of porous media. The effective diffusivity of mixed gases has been measured using techniques including gas chromatography (GC) [5,6], steady-state diffusion cells, transient diffusion cells, thermo-gravimetry using a microbalance [7], and zero-length columns [8]. Measurements of effective diffusivity by all of these methods are conducted at a pressure of one atmosphere and in the temperature range from 30 to 300^{o}C. From the standpoint of SOFC, however, the more interesting value of O_2-N_2 effective diffusivity is that measured at 800^{o}C, which is the typical operating temperature of anode-supported SOFC.

[2] In Knudsen diffusion dominated flow, the pore radius (assumed cylindrical) is equal to or less than the molecular mean free path, such that gas molecules collide more frequently with pore walls than with other molecules.

In this study, the effective binary diffusivity of O_2-N_2 through porous media was measured over a range of temperatures between 650 and 800°C using an electrochemical concentration cell. Measurements were conducted on porous discs of Sr-doped $LaMnO_3$ with total porosity ranging between 29 and 48%. The electrochemical cell allowed for an accurate control of the oxygen partial pressure within the sealed cell chamber. Thus, one side of the porous membrane was exposed to ambient conditions (p_{O_2} = 0.21 atm) while the oxygen partial pressure on the other side was carefully regulated with the concentration cell. The effective binary diffusivity of O_2-N_2 was calculated based on the measured oxygen flux through the porous membrane under steady-state conditions.

II. THEORETICAL ANALYSIS

Analysis of gas transport through porous bodies can be done using the method of effective diffusivities, which explicitly accounts for pore volume and tortuosity, or using the Dusty gas model, in which the material comprising the solid part of the porous body is treated as an additional gaseous species with enormous mass, and thus is effectively immobile [9]. In what follows, we will use the method of effective diffusivities.

Isothermal, binary transport of O_2 and N_2 through a porous medium can be phenomenologically described by the following equations (wherein 1 denotes O_2 and 2 denotes N_2) [9],

$$J_1 = -D_1 \nabla n_1 + X_1 \delta_1 J - X_1 \gamma_1 \left(\frac{nB_o}{\mu}\right) \nabla p \qquad (1)$$

$$J_2 = -D_2 \nabla n_2 + X_2 \delta_2 J - X_2 \gamma_2 \left(\frac{nB_o}{\mu}\right) \nabla p \qquad (2)$$

where $$\delta_1 = \frac{D_{1K}^{eff}}{D_{1K}^{eff} + D_{12}^{eff}} \quad \text{and} \quad \delta_2 = \frac{D_{2K}^{eff}}{D_{2K}^{eff} + D_{12}^{eff}} \tag{3}$$

$$\gamma_1 = 1 - \delta_1 = \frac{D_{12}^{eff}}{D_{1K}^{eff} + D_{12}^{eff}} \quad \text{and} \quad \gamma_2 = 1 - \delta_2 = \frac{D_{12}^{eff}}{D_{2K}^{eff} + D_{12}^{eff}} \tag{4}$$

$$\frac{1}{D_1} = \frac{1}{D_{1K}^{eff}} + \frac{1}{D_{12}^{eff}} \quad \text{and} \quad \frac{1}{D_2} = \frac{1}{D_{2K}^{eff}} + \frac{1}{D_{12}^{eff}} \tag{5}$$

where n_1, and n_2 are the concentrations of 1 and 2 (in #/m^3 or #/cm^3), respectively, X_1 and X_2 are the mole fractions of 1 and 2, respectively, n is the total concentration, μ is viscosity (Pa-sec or dyne-sec), B_o is permeability (m^2 or cm^2), P is total pressure (N/m^2 or dyne/cm^2), J_1 and J_2 are the fluxes of 1 and 2, respectively, J is the total flux, D_{1K}^{eff} and D_{1K}^{eff} are the effective Knudsen diffusivities of 1 and 2, respectively (m^2/sec or cm^2/sec), and D_{12}^{eff} is the effective binary diffusivity. The effective Knudsen diffusivities, D_{1K}^{eff} and D_{1K}^{eff}, are related to the Knudsen diffusivities, D_{1K} and D_{2K}, by

$$D_{1K}^{eff} = \frac{D_{1K} V_v}{\tau} \text{ and } D_{2K}^{eff} = \frac{D_{2K} V_v}{\tau} \tag{6}$$

where V_v is the volume percent of porosity and τ is the tortuosity factor.

If the pore size is sufficiently large, the effects of Knudsen diffusion may be neglected. Thus, if D_{1K}^{eff} and $D_{2K}^{eff} >> D_{12}^{eff}$, the flux equations reduce to:

$$J_1 = -D_{12}^{eff} \nabla n_1 + X_1 J - \frac{X_1 n D_{12}^{eff}}{D_{1K}^{eff}} \frac{B_0}{\mu} \nabla p \tag{7}$$

$$J_2 = -D_{12}^{eff}\nabla n_2 + X_2 J - \frac{X_2 n D_{12}^{eff}}{D_{2K}^{eff}}\frac{B_0}{\mu}\nabla p \qquad (8)$$

In the above, we have replaced $D_{1K}^{eff} + D_{12}^{eff}$ and $D_{2k}^{eff} + D_{12}^{eff}$ by, respectively, D_{1K}^{eff} and D_{2K}^{eff}. Consider the application of above equations to a solid oxide fuel cell (SOFC) cathode. When an SOFC is operated under load, a net current density flows through the cell. The corresponding flux of molecular oxygen flows from the cathodic chamber, through the porous cathode, to the cathode/electrolyte interface, where oxygen molecules are converted into oxygen ions, and are incorporated into the electrolyte for further transport towards the anode. In a steady state, the partial pressure of oxygen at the cathode/electrolyte interface will be fixed, and will be a function of porosity, tortuosity factor, thickness, and the current density. The transport of oxygen through the porous cathode can then be described by equation (7). The flux of nitrogen, similarly, is described by equation (8). However, no net transport of nitrogen can occur through the electrolyte, as the electrolyte only conducts oxygen ions. Under a steady state, therefore, nitrogen flux must be zero everywhere. That is, under a steady state, $J_2 = 0$ since the nitrogen flux is zero. Thus, Equation (7) can be rewritten as

$$J_1 = -D_{12}^{eff}\nabla n_1 + X_1 J_1 - \frac{X_1 n D_{12}^{eff}}{D_{1K}^{eff}}\frac{B_o}{\mu}\nabla p \qquad (9)$$

and equation (8) as

$$0 = -D_{12}^{eff}\nabla n_2 + X_2 J_1 - \frac{X_2 n D_{12}^{eff}}{D_{2K}^{eff}}\frac{B_o}{\mu} \qquad (10)$$

Adding equations (9) and (10),

$$J_1 = -D_{12}^{eff}\nabla(n_1 + n_2) + (X_1 + X_2)J_1 - \frac{X_1 n D_{12}^{eff}}{D_{1K}^{eff}}\frac{B_o}{\mu}\nabla p - \frac{X_2 n D_{12}^{eff}}{D_{2K}^{eff}}\frac{B_o}{\mu}\nabla p \qquad (11)$$

Assuming the applicability of the ideal gas equation of state, we have

$$n_1 = \frac{p_1}{k_B T} \quad , \quad n_2 = \frac{p_2}{k_B T} \quad \text{and} \quad n = n_1 + n_2 = \frac{p_1}{k_B T} + \frac{p_2}{k_B T} = \frac{p}{k_B T} \tag{12}$$

where, k_B is the Boltzmann constant. We also know that $X_1 + X_2 = 1$. Substitution into equation (11) gives

$$0 = \left[\frac{D_{12}^{eff}}{k_B T} + \frac{X_2 n D_{12}^{eff}}{D_{2K}^{eff}} \frac{B_0}{\mu} + \frac{X_1 n D_{12}^{eff}}{D_{1K}^{eff}} \frac{B_0}{\mu} \right] \nabla p \tag{13}$$

Equation (13) implies that $\nabla p = 0$ and the flux equations reduce to

$$J_1 = -D_{12}^{eff} \nabla n_1 + X_1 J_1 \tag{14}$$

or

$$J_1 = \frac{-D_{12}^{eff}}{(1 - X_1)} \nabla n_1 \tag{15}$$

Using Equation (12), the flux J_1 is given by,

$$J_1 = \frac{-D_{12}^{eff}}{k_B T} \frac{p}{(p - p_1)} \nabla p_1 \tag{16}$$

The flux of oxygen molecules, J_1 (mol·cm^{-2}·sec^{-1}) is related to current density by,

$$J_1 = \frac{i}{4F} \tag{17}$$

where i is current density and F is the Faraday constant.

Substitution into Equation (16) for one-dimensional transport gives

$$\frac{iN_A k_B T dx}{4FD_{12}^{eff} p} = \frac{-dp_1}{(p - p_1)} \tag{18}$$

where N_A is Avogadro's number. In an actual SOFC, it is not possible to measure the partial pressure of oxygen at the cathode/electrolyte interface. However, transport characteristics of the cathode can be independently and experimentally investigated by an electrochemical cell of the type shown in Figure 1(a), which is a schematic of the electrochemical cell used in this study for the measurement of the O_2-N_2 effective diffusivity. The electrochemical cell consists of a disc of an oxygen ion conducting material (e.g. yttria-stabilized zirconia or YSZ), sealed to a YSZ cylinder using a suitable glass. Platinum electrodes are applied to both the disc as well as part of the cylinder, as shown in Figure 1(a). At the other end, a porous disc of a prospective cathode is attached, again using a suitable glass. The entire assembly is heated to an elevated temperature, and a DC voltage is applied across the electrodes on the YSZ disc, so as to pump out oxygen from the cylinder. As the partial pressure of oxygen in the cylinder (p_i or pO_2) is lowered, oxygen from the ambient diffuses through the porous disc, into the chamber (cylinder). Under a steady state, the pO_2 in the cylinder is lower than that in the ambient. This pO_2 can be measured electrochemically using the electrodes applied to the YSZ cylinder, which serve as sensing electrodes. The flux of oxygen through the porous disc is described by the preceding equations. Also, as no nitrogen can transport through the YSZ disc, it is clear that under a steady state, no transport of nitrogen occurs through the porous disc. In this sense, the electrochemical cell simulates conditions experienced by an SOFC cathode, with the opportunity to precisely know what the pO_2 in the cylinder is; or what the pO_2 at the cathode/electrolyte interface is in an actual SOFC, under a given set of conditions.

Figure 1(b) shows a schematic of a porous LSM disc, with the thickness and the partial pressures of oxygen labeled. From Figure 1(b), when $x = 0$, the oxygen partial pressure outside of the zirconia tube is, $p_1 = p_0$, and when $x = l$, the oxygen partial pressure inside of the zirconia tube is, $p_1 = p_i$, and p = total pressure. Integration of Equation (18) gives

$$p_i = p - (p - p_0)\exp\left[\frac{iRTl}{4FD_{12}^{eff}\,p}\right] \tag{19}$$

where R is the ideal gas constant. Since the thickness of the porous LSM disk is small, the exponent can be shown to be much less than one, for most current densities of interest. Then Equation (19) can be simplified as

$$p_i \approx p_0 - (\frac{p - p_0}{p})\left[\frac{iRTl}{4FD_{12}^{eff}}\right] \tag{20}$$

Substituting for $\frac{i}{4F}$ with J in Equation (20) gives

$$J \approx -\left[\left(\frac{p}{p - p_0}\right)\cdot\left(\frac{D_{12}^{eff}}{RTl}\right)\right](p_i - p_0) = \left(\frac{pp_0}{p - p_0}\right)\left(\frac{D_{12}^{eff}}{RTl}\right) - \left(\frac{p}{p - p_0}\right)\left(\frac{D_{12}^{eff}}{RTl}\right)p_i \tag{21}$$

where p = 1 atm (1.013 x 10^5 N/m^2), p_0 = 0.21 atm (2.128 x 10^4 N/m^2), p_i is the oxygen partial pressure inside the electrochemical cell, l is the thickness of the porous LSM disk, T is the operating temperature, and D_{12}^{eff} is the O_2-N_2 effective binary diffusivity, $D_{O_2-N_2}^{eff}$.

From the slope of oxygen flux through the porous LSM sample as a function of partial pressure of oxygen inside the cell, p_i, the O_2-N_2 effective diffusivity, $D_{O_2-N_2}^{eff}$, through the porous disc can be calculated. Equation (21) shows that the $D_{O_2-N_2}^{eff}$ can also be obtained from the intercept.

III. EXPERIMENTAL PROCEDURE

Fabrication of Porous LSM Discs: Porous samples in the shape of discs were fabricated from $La_{0.85}Sr_{0.15}MnO_3$ powder (Praxair), mixed with 20%, 22.5%, 25%, 27.5% and 30% (by weight) carbon (HTW). Carbon particles were spherical with a particle size ranging between 20 and 50 μm in diameter. The powder mixtures were wet-milled, dried, and then screened. Discs of diameter ~20 mm and thickness ~1 mm were uniaxially die-pressed and then fired at 1200°C for one hour in air. The microstructure and porosity of the samples were evaluated using scanning electron microscopy (SEM). The open, closed, and total porosity of the samples was measured by the Archimedes technique in accordance with ASTM Standard C 20-00.

Design and Construction of the Diffusivity Measurement Set-Up: The O_2-N_2 effective diffusivity through the porous discs was measured using an electrochemical concentration cell. The cell was fabricated using a dense, 8 mol.% yttria-doped zirconia (YSZ) cylindrical tube, a dense YSZ disc, and a porous LSM disc, as shown in Figure 1(a). Platinum electrodes, in the form of a paste, were applied on both sides of the YSZ disc, and both sides of the YSZ cylinder, on part of the surface. Platinum wire leads were attached to both sets of platinum electrodes. The YSZ cylinder and disc were heated to 750°C for one hour to ensure that the platinum wire and paste were well adhered to the YSZ disc and the YSZ cylinder. A glass frit (Specialty Glass, Inc.) was mixed with an organic binder to form a paste. The paste was applied between the YSZ cylinder (edge) and disc and the assembly was fired at 850°C for 4 hours to form a leak-tight seal. The porous LSM disk was sealed to the other end of the YSZ cylinder using the same procedure. This completed the fabrication of the electrochemical cell.

Electrochemical Measurements: The electrochemical cell was placed in a furnace and measurements were conducted over a range of temperatures between 650 and 800°C. The platinum leads from the YSZ disc were attached to a constant voltage/current DC power supply. In this manner, oxygen could be electrochemically pumped in or out of the cell, depending upon the polarity. The applied current from the power source was monitored using a Keithly Model 2000 multimeter. The oxygen pump was operated in both

directions to either pump oxygen in or out of the cell. The platinum leads from the zirconia cylinder were connected to a Keithly Model 2000 multimeter linked to a computer with LabView software for data acquisition. The Nernst potential of the oxygen sensor was continuously measured. Thus, the partial pressure of oxygen inside the cell was known as a function of time. In terms of the measured Nernst potential, E, and the oxygen partial pressure in the ambient, p_0, the oxygen partial pressure in the chamber, p_i, is given by

$$p_i = p_0 \exp\left[-\frac{4FE}{RT}\right] \tag{22}$$

When the applied polarity is such that oxygen is electrochemically pumped out, the E is positive and $p_i < p_0$. During testing, a constant current was applied to the pump and the Nernst voltage was monitored until the oxygen partial pressure inside the cell reached a stable (steady state) value. Testing was repeated with the oxygen sensor placed in various locations to ensure that the oxygen partial pressure gradient in the zirconia tube was negligible. The oxygen partial pressure inside the cell was controlled by varying the magnitude of the current applied to the oxygen pump.

IV. RESULTS AND DISCUSSION

Microstructural Characterization of Porous Discs: Figure 2 shows an SEM micrograph of a porous LSM sample in which 27.5 wt.% carbon was added to the powder prior to sintering. The size of the pores, as estimated from the micrographs, varied between 1.5 μm and 50 μm in diameter, with the mean pore size (diameter) being approximately 10 to 15 μm in diameter. The smaller pores are the result of the breakage of large carbon particles during the milling process. Very small pores are the result of partial sintering, and the corresponding pore sizes are related to the LSM particle size.

The density, and open, closed, and total porosities of the LSM discs fabricated with 20 to 30 wt.% carbon, as measured by the Archimedes technqiue, are presented in Table I. In addition, the total porosity, as calculated by SEM image analysis (systematic point count), is also listed in Table I. With increasing amounts of carbon from 20 wt.% to 30 wt.%, the density decreases from 4.64 g/cm^3 to 3.41 g/cm^3, the total porosity increases from 28.9% to 47.7%, and the open porosity increases from 15.4% to 43.7%. The amount of closed porosity decreases from 13.4% to 4.3% with increasing carbon content from 20 to 25 wt.%, and then remains relatively constant at higher carbon concentrations. Thus, there appears to be a critical amount of carbon necessary to ensure that most of the porosity is open[3]. For the given morphology of carbon and resulting pore shape and size, this critical amount lies between 22.5 and 25.0 wt.%. At carbon contents greater than or equal to 25 wt.%, approximately 90 percent of the total porosity is open.

The Effect of Porosity on the Effective Binary Diffusivity of O_2-N_2: The effective binary diffusivity, $D^{eff}_{O_2-N_2}$, was determined by measuring the oxygen flux through porous samples as a function of oxygen partial pressure gradient across the sample. For each flux measurement, a constant current was applied, and maintained until the electrochemical cell reached a steady state, before proceeding to the next measurement. Figure 3 shows a typical plot of Nernst potential as a function of time for a porous disc sample with 24.4% open porosity. The pump current was set at 106.6 mA and the cell reached steady state in approximately 5 minutes. The plots of oxygen flux as a function of oxygen partial pressure in the cell (inside the YSZ cylinder) for porous LSM samples fabricated with 20 to 30 wt.% carbon are shown in Figure 4. The oxygen flux as a function of oxygen partial pressure, p_i, in the cell, exhibits linear behavior over the range of p_i measured. Linear dependence of oxygen flux on p_i suggests that the simplification given in equation (21) is valid, and that over the range of measurements, $D^{eff}_{O_2-N_2}$, for a given sample is essentially a constant. The O_2-N_2 binary effective diffusivity, $D^{eff}_{O_2-N_2}$, for transport through the

[3] It is to be emphasized that this conclusion concerning the required amount of carbon is valid only for sintered LSM discs, as in the current study, and not for cathode, as applied on SOFC. This is because in the case of discs, sintering is not constrained. However, in a typical SOFC, the cathode is applied over an already fabricated cell, which leads to constrained sintering, and thus greater porosity.

porous samples was determined using Equation (21), both from the slope as well as the intercept. The corresponding results are listed in Table II. Note that with the exception of the sample with the lowest porosity, the $D^{eff}_{O_2-N_2}$ measured from both the slope and the intercept, are virtually identical. This demonstrates the validity of the analysis, and the experimental procedure. At the lowest porosity, the value estimated from the intercept is somewhat greater. In the following discussion, the values of $D^{eff}_{O_2-N_2}$ estimated from the slope are used. The effective diffusivity increases from 0.016 cm^2/s to 0.12 cm^2/s with increasing porosity in the range 15.4% to 43.8%. The dependence of O_2-N_2 effective binary diffusivity on open porosity is nonlinear, as shown in Figure 5.

The total gas transport through a porous sample should contain contributions from bulk diffusion, Knudsen diffusion, and viscous flow (Equations 1 and 2), in addition to surface diffusion and adsorption/desorption-related effects. In the preceding, it was assumed that the effective Knudsen diffusivities ($D^{eff}_{O_2K}$, $D^{eff}_{N_2K}$) are much larger than the effective binary diffusivity ($D^{eff}_{O_2-N_2}$). With this assumption, the pressure gradient across the sample was shown to be equal to zero ($\nabla p = 0$) resulting in no viscous flow through the porous cathode. Thus, the effective diffusivity, $D^{eff}_{O_2-N_2}$, calculated from Equation (21) is valid if the Knudsen diffusion in the porous LSM samples can be neglected, and effects due to surface diffusion and adsorption/desorption processes are small.

The important parameters in determining the relative contributions of Knudsen and bulk diffusion to total diffusion are the pore size and the mean free path of the gaseous species. Bulk diffusivity is a function of the molecular velocity υ and the mean free path λ as given by [10],

$$D_{12} = \frac{1}{3}\upsilon\lambda \tag{23}$$

Knudsen diffusivity is dependent on the molecular velocity υ and the radius a of a cylindrical pore as given by [10],

$$D_K = \frac{2}{3}\upsilon a \tag{24}$$

The mean free path λ of many gases at one atmosphere is usually on the order of 100 nm at the temperature of interest (~800°C) [11]. For the porous LSM samples (Figure 2) the mean pore radius, as measured from micrographs, is about 5 μm.[4] Thus, as given by Equations (23) and (24), $D^{eff}_{O_2K}$ and $D^{eff}_{N_2K}$ will be an order of magnitude greater than $D^{eff}_{O_2-N_2}$. Therefore, at a total pressure of 1 atmosphere, bulk diffusion should dominate and the assumption that Knudsen diffusion can be neglected appears to be valid.

In the phenomenological theory of diffusion through porous bodies, the O_2-N_2 effective diffusivity, $D^{eff}_{O_2-N_2}$, is related to the O_2-N_2 binary bulk diffusivity by [12],

$$D^{eff}_{O_2-N_2} = \frac{V_V}{\tau} D_{O_2-N_2} \tag{25}$$

where V_V is the volume percent of porosity and τ is the tortuosity factor. The experimentally measured tortuosity factor is an all-encompassing term that includes the effects of pore microstructure, such as pore orientation, morphology, contiguity, and size, as well as possible adsorption/desorption processes, and surface diffusion, etc., on gas transport. The volume percent of porosity accounts for the fact that gas transport occurs only through the pores and not through the solid matrix.

The bulk diffusivity of a binary gas system at moderate temperatures and pressures can be accurately determined by the Chapman-Enskog relation [12] given as,

$$D_{O_2-N_2} = \frac{0.00186T^{\frac{3}{2}}\left(\frac{1}{M_{O_2}} + \frac{1}{M_{N_2}}\right)^{\frac{1}{2}}}{p\sigma^2_{O_2-N_2}\Omega} \tag{26}$$

[4] The bottlenecks are almost certainly smaller than pore radii determined from micrographs. Thus, the above leads to an overestimate of the Knudsen diffusivity.

in cm^2/sec where M_{O_2} and M_{N_2} are the molecular weights of the two gaseous species, Ω is the collision integral, $\sigma_{O_2-N_2}$ is the average collision diameter, and p is the total pressure. The collision diameter $\sigma_{O_2-N_2}$, given in angstroms, is the arithmetic average of the diameters of the two species present:

$$\sigma_{O_2-N_2} = \frac{1}{2}\left(\sigma_{O_2} + \sigma_{N_2}\right) \tag{27}$$

The collision integral Ω is a dimensionless quantity that accounts for interaction between the two gaseous species via the Lennard-Jones potential. For the binary gas system of O_2-N_2 at 800°C, the collision integral is close to unity [12]. The bulk diffusivity of O_2-N_2 as determined by Equation (26), is approximately 2.08 cm^2/s at 800°C and 1 atm.

Based on the calculated O_2-N_2 bulk diffusivity (Equation (26)), the measured effective O_2-N_2 diffusivity (Table II), and the volume percent of porosity (Table I), the tortuosity factor, τ, can be estimated by Equation (25). The calculated tortuosity factors for the porous LSM samples fabricated with 20 to 30 wt.% carbon are presented in Table II. The tortuosity factor decreases from a value of 19.7 to 7.8 with increasing carbon content from 20 to 30 wt.%. The tortuosity factor decreases with increasing open porosity in a non-linear manner as shown in Figure 6. Typically, the tortuosity factor of porous media lies between 2 and 6, but values as high as 10 have been reported [11]. The estimated tortuosity factors of the LSM samples fabricated with 20, 22.5 and 25 wt.% carbon were high with values ranging between 15.6 and 19.7. Such high values of tortuosity factors are probably the result of neglecting Knudsen diffusion, surface diffusion and adsorption/desorption processes. It is quite possible that the dimensions of bottlenecks in the pore structure may be considerably smaller than the estimated average size of pores from SEM micrographs. This would mean that the actual Knudsen diffusivities are probably smaller than assumed, and high tortuosity factors are the result of neglecting the effects of Knudsen diffusion.

For evaluating the Knudsen diffusivity given in Equation (24), the following expression was used to determine the mean molecular velocity of a gas species in a mixture [11],

$$\upsilon_1 = \sqrt{\frac{8RT}{\pi M_1}} \tag{28}$$

where M_1 is the molecular weight of component 1 in a mixture.

Combining Equation (24) with Equation (28) gives,

$$D_K = \frac{2}{3} a \sqrt{\frac{8RT}{\pi M_1}} \tag{29}$$

Combining Equation (25) with Equation (29) gives the effective Knudsen diffusivity for each gaseous species in the mixture,

$$D_{1K}^{eff} = \frac{2}{3} a \sqrt{\frac{8RT}{\pi M_A}} \frac{V_v}{\tau} \tag{30}$$

and

$$D_{2K}^{eff} = \frac{2}{3} a \sqrt{\frac{8RT}{\pi M_B}} \frac{V_v}{\tau} \tag{31}$$

where M_1 and M_2 are the molecular weights of gaseous species 1 and 2, respectively.

Knowing the tortuosity factor, the effective Knudsen diffusivities of both O_2 and N_2 through the porous LSM samples can be determined by Equations (30) and (31) assuming some pore radius. In the present work, the pore size was estimated from SEM micrographs. However, the actual pore bottlenecks are almost certainly smaller. Thus, the present calculations of Knudsen diffusivities are overestimates.

The calculated O_2 and N_2 effective Knudsen diffusivities for the porous LSM samples at 800^{o}C and 1 atm are listed in Table II. The calculated Knudsen diffusivities increase from 0.23 to 1.68 for the samples fabricated from 20 to 30 wt.% carbon. For all samples, both the $D_{O_2K}^{eff}$ and $D_{N_2K}^{eff}$ are an order of magnitude greater than $D_{O_2-N_2}^{eff}$, which is consistent with the original assumption. However, it is to be emphasized that the actual bottlenecks may be smaller than the assumed pore sizes. If this is the case, large tortuosity factors

estimated for samples of lower porosity, may principally be the result of neglecting the effects of Knudsen diffusion.

The Temperature Dependence of the Effective Binary Diffusivity of O_2-N_2: The effective diffusivities of O_2-N_2 through porous media at various temperatures were measured. The effective diffusivities for the samples fabricated with 22.5 wt.% carbon and 27.5 wt.% carbon at temperatures between 650 and 800°C are listed in Table III. As seen in the table, the $D^{eff}_{O_2-N_2}$ increases with increasing temperature. The increase in effective diffusivity with temperature is due to the increase in the average molecular velocity and the mean free path. As a function of temperature T, the average molecular velocity follows a $T^{0.5}$ dependence and the mean free path is linear with T. Thus, the effective diffusivity should exhibit a $T^{1.5}$ dependence. The effective diffusivity for both samples plotted as a function of $T^{1.5}$ is shown in Figure 7. The effective diffusivities are linear with respect to $T^{1.5}$ consistent with the Chapman-Enskogg relation. The intercept, however, should be zero. The observation that the intercept is nonzero is simply the result of experimental scatter in measurements. The slope of the sample fabricated from 27.5 wt.% carbon is greater than that for the sample fabricated from 22.5 wt.% carbon by a factor of 2.5. The difference in slopes is partially attributed to the higher percentage of porosity and a lower value of tortuosity in the samples made with 27.5 wt.% carbon as compared to the samples made with 22.5 wt.% carbon. A comparison of the ratios $\frac{V_V}{\tau}$ for the two samples at 800°C (Table II) shows that they differ by a factor of approximately 1.9.

The Limiting Current Density and Concentration Polarization: The limiting current density due to concentration polarization at the cathode is determined by setting Equation (20) to zero, i.e. $p_i \approx 0$, and is given by,

$$i_{cs} \approx \left[\frac{4FD^{eff}_{O_2-N_2}}{RTl}\right] p_o \left(\frac{p}{p-p_o}\right) \tag{32}$$

where p_o is the partial pressure of oxygen in the oxidant (air) outside of the cathode (Pa or atm), p is total pressure, D_{12}^{eff} is the effective O_2-N_2 diffusion coefficient of the porous cathode (cm^2/s or m^2/s), and l is the cathode thickness (cm or m). If the more accurate equation (equation (19)) is used instead, the limiting current density is given by

$$i_{cs} \approx \left[\frac{4FD_{O_2-N_2}^{eff}}{RTl} \right] p \ln\left(\frac{p}{p - p_o} \right) \tag{33}$$

In practice, limiting current densities given by equations (32) or (33) often may not be realized since limiting current densities due to either the ohmic contribution or the anodic polarization may smaller. For example, in an electrolyte-supported cell, the ohmic polarization is usually the largest. In such a case, the short circuit current density occurs mainly due to the fact that almost all voltage drop is attributable to the ohmic polarization. The limiting current densities given in equations (32) and (33), are useful for estimating the contributions of cathodic concentration polarization as a function current density.

In terms of the limiting current density, i_{cs}, the concentration polarization at the cathode is given as [13],

$$\eta_{conc(c)} = -\frac{RT}{4F} \ln\left(1 - \frac{i}{i_{cs}} \right) \tag{34}$$

where i is current density (A/cm^2). Assuming that the cathode of an anode-supported solid oxide fuel cell has a similar microstructure as the porous LSM disc samples, the cathode limiting current density and cathode polarization can be estimated by Equations (32) or (33), and (34). Table IV lists the cathode limiting current densities calculated for different effective diffusivities for cathodes of two different thicknesses; 50 μm and 200 μm. The cathode concentration overpotential as a function of current density (up to 2 A/cm^2) for cathodes with various effective diffusivities is shown in Figure 8(a) and Figure 8(b) for cathode thicknesses of 50 and 200 μm, respectively. Note that there is a significant effect of cathode porosity on concentration polarization, especially for the cathode thickness of 200 μm. Thus, the effective diffusivity of O_2-N_2 in porous cathodes can greatly influence the overall performance of a cell.

The effects of cathode thickness and porosity on the cathode overpotential are shown in Table V. The overpotentials were calculated based on the O_2-N_2 effective diffusivities of the porous LSM samples. For the sample fabricated with 20 wt.% carbon, the cathode overpotential increases from 7.1 mV to 86.2 mV with an increase in cathode thickness from 50 to 200 μm for a current density of 2 A/cm^2. On the other hand, for the 30 wt.% carbon sample, the cathode overpotential only increases from 0.9 mV to 3.7 mV when increasing the cathode thickness from 50 to 200 μm. Thus, the adverse effects of increasing cathode thickness on concentration polarization are greatly reduced with adequate porosity.

V. CONCLUSIONS

The present work has developed an electrochemical technique, which affords the measurement of effective binary diffusivities of O_2-N_2, $D^{eff}_{O_2-N_2}$, through porous media at elevated temperatures. The technique was applied to porous LSM discs containing a range of porosities, and as a function of temperature between 650 and 800^{o}C. The results showed that transport through porous LSM discs could be adequately described by effective binary diffusion. The O_2-N_2 effective binary diffusivity, $D^{eff}_{O_2-N_2}$, at 800°C increased from ~0.016 to ~0.12 cm^2/s with increasing open porosity between 15 and 44 vol.%. Using the values of the effective diffusivities measured, cathodic concentration polarization was estimated. The results show that for relatively thick cathodes (~200 microns), cathodic concentration polarization can be significant, especially at lower porosities. This shows the importance of ensuring that the open porosity in the cathode is adequate. Also using the experimentally measured $D^{eff}_{O_2-N_2}$, the volume fraction of porosity, and the calculated binary diffusivity by the Chapman-Enskog model, tortuosity factors were estimated. The estimated tortuosity factor ranged between ~7.8 and ~19.7, the latter for samples with relatively low porosity. At high values of porosity, the

estimated tortuosity factor (~7.8) may be attributed to the tortuous nature of gas transport. Very high tortuosity factors (such as >10), in samples with a low volume fraction of open porosity, are probably the result of neglecting Knudsen diffusion and surface diffusion. In these samples, it is possible that the pore size, especially the bottlenecks, may be on the order of the mean free path.

ACKNOWLEDGMENTS

This work was supported by the U.S. Department of Energy, NETL, Contract No. DE-AC26-99FT40713.

REFERENCES

1. K.Z. Fung and A. V. Virkar, in *Proceedings of the 4th Internaional Symposium on Solid Oxide Fuel Cells (SOFC-IV)*, M. Dokiya, O. Yamamoto, H. Tagawa, and S. C. Singhal, Editors, PV95-1, p. 1105, The Electrochemical Society Proceedings Series, Pennington, NJ (1995).
2. T. Kenjo and Y. Yamakoshi, *Bull. Chem. Soc. Jpn*., **65**, 995 (1992).
3. C. N. Satterfield, *Mass Transfer in Heterogeneous Catalysis*, MIT Press, Cambridge, MA, 1970.
4. R. Aris, *The Mathematical Theory of Diffusion and Reaction in Permeable Catalysts*, Clarendon Press, Oxford, 1975.
5. P. Schneider and J.M. Smith, *AIChE J.*, **14**, 762 (1968).
6. E. Ruckenstein, A. S. Vaidyanathan, and G. R. Youngquist, *Chem. Eng. Sci.*, **25**, 1306 (1971).
7. P. Gray and D. D. Do, *AIChE J.*, **37**, 1027 (1991).
8. J. R. Hufton and D. M. Ruthven, *Ind. Eng. Chem. Res.*, **32**, 2379 (1993).
9. E. A. Mason and A. P. Malinaukus, *Gas transport in porous media: The dusty gas model, Elsevier*, Amsterdam, (1983).
10. J. M. Smith, *Chemical Engineering Kinetics*, McGraw-Hill Book Company, (1970).
11. F. P. Reif, '*Statistical and Thermal Physics*', McGraw-Hill, New York (1975).
12. E. L. Cussler, '*Diffusion*: *Mass transfer in fluid systems*', Cambridge University Press, Cambridge (1995).
13. J. W. Kim, A. V. Virkar, K-Z. Fung, K. Metha, and S. C. Singhal, *J. Electrochem. Soc.*, **146** [1], 69-78 (1999).

FIGURE CAPTIONS

Figure 1(a). A schematic of the electrochemical cell used to measure the effective binary diffusivity, $D^{eff}_{O_2-N_2}$, in porous samples.

Figure 1(b). A schematic of a LSM porous disc, along with partial pressures of oxygen.

Figure 2. A scanning electron micrograph (SEM) of a porous LSM disc fabricated with 27.5 wt.% carbon.

Figure 3. The measured Nernst potential across the oxygen sensor as a function of time, under a constant applied current to the pump made using a LSM disc with 24.4% porosity. Measurement conducted at 800°C.

Figure 4. Oxygen flux through porous LSM discs fabricated with varying amounts of carbon, between 20.0 wt.% and 30.0 wt.%, as a function of oxygen partial pressure inside the cell. Measurement conducted at 800°C.

Figure 5. Effective binary diffusivity, $D^{eff}_{O_2-N_2}$, vs. open porosity.

Figure 6. Tortuosity factor vs. open porosity.

Figure 7. Effective binary diffusivity, $D^{eff}_{O_2-N_2}$, as a function of temperature, $T^{1.5}$, for porous LSM disks fabricated with 22.5 and 27.5 wt.% carbon.

Figure 8(a). Calculated cathode overpotential as a function of current density for porous LSM cathodes fabricated with 20.0 to 30.0 wt.% carbon. Cathode thickness = 50 microns. Cathode-limiting current density calculated using equation (32).

Figure 8(b). Calculated cathode overpotential as a function of current density for porous LSM cathodes fabricated with 20.0 to 30.0 wt.% carbon. Cathode thickness = 200 microns. Cathode-limiting current density calculated using equation (32).

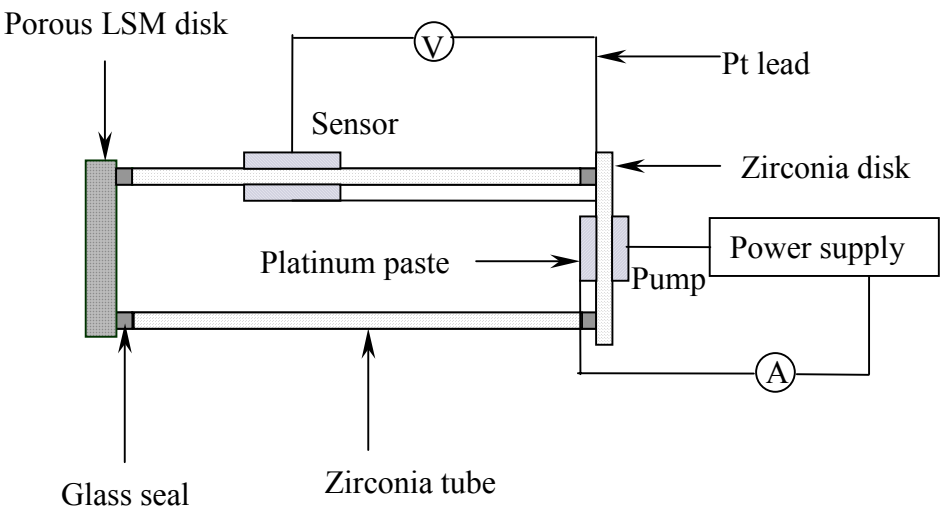

Figure 1(a). A schematic of the electrochemical cell used to measure the effective binary diffusivity, $D^{eff}_{O_2-N_2}$, in porous samples.

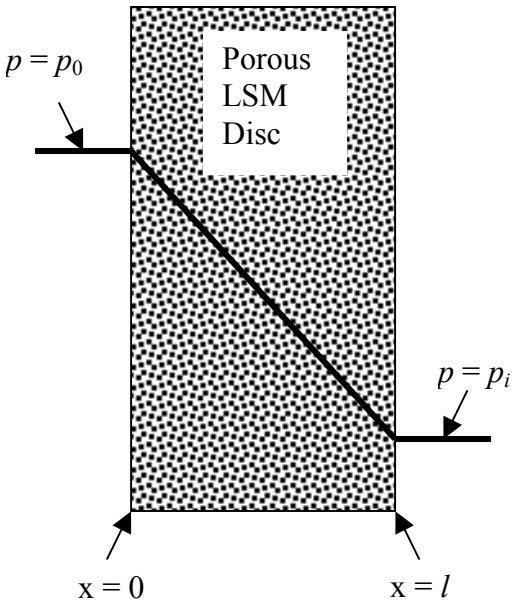

Figure 1(b). A schematic of a LSM porous disc, along with partial pressures of oxygen.

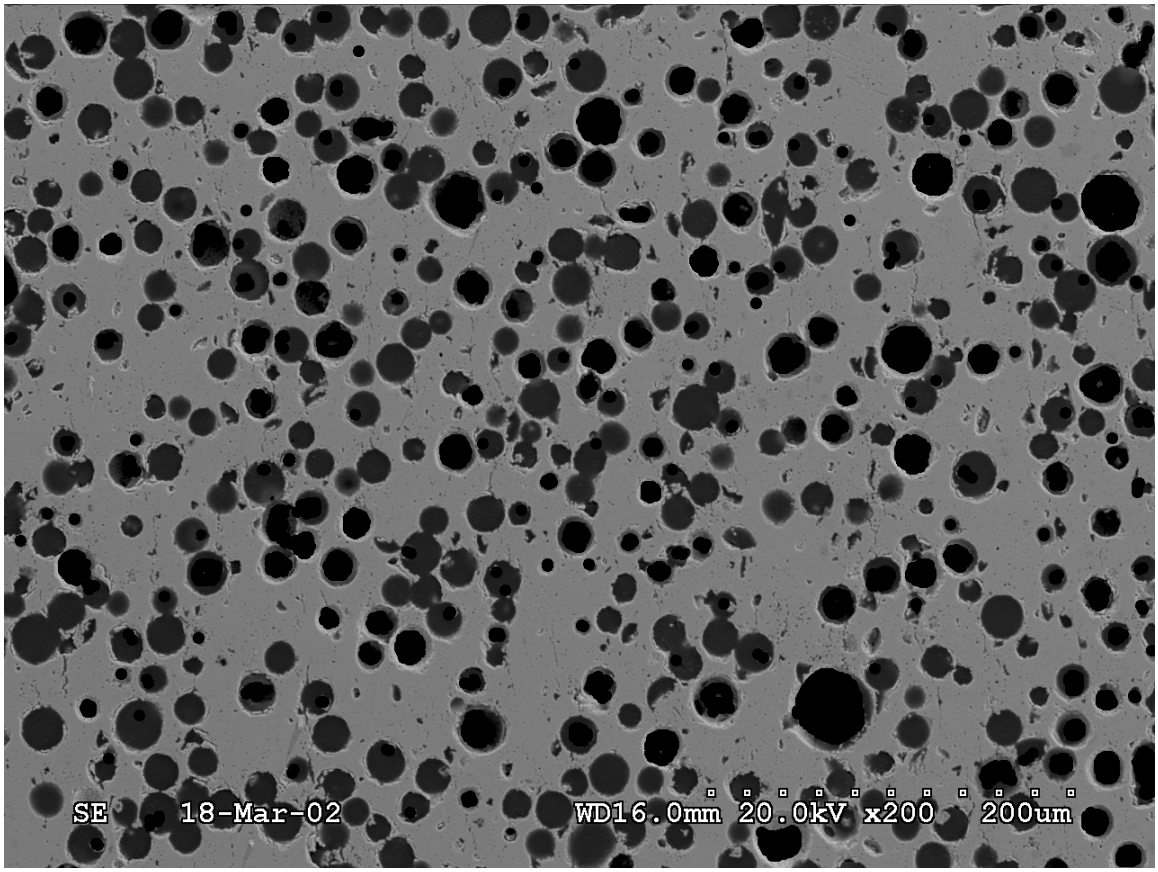

Figure 2. A scanning electron micrograph (SEM) of a porous LSM disc fabricated with 27.5 wt.% carbon.

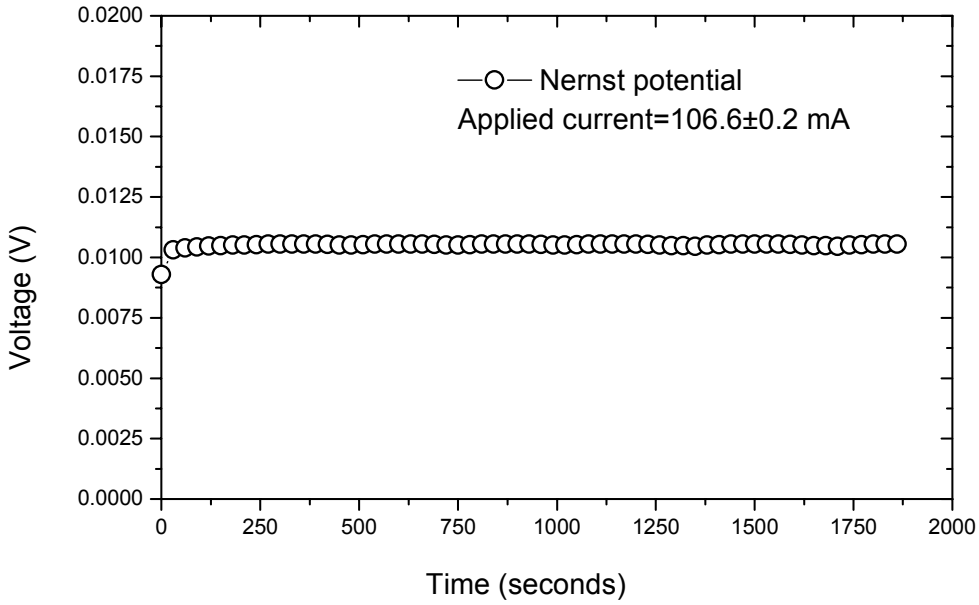

Figure 3. The measured Nernst potential across the oxygen sensor as a function of time, under a constant applied current to the pump made using a LSM disc with 24.4% porosity. Measurement conducted at 800°C.

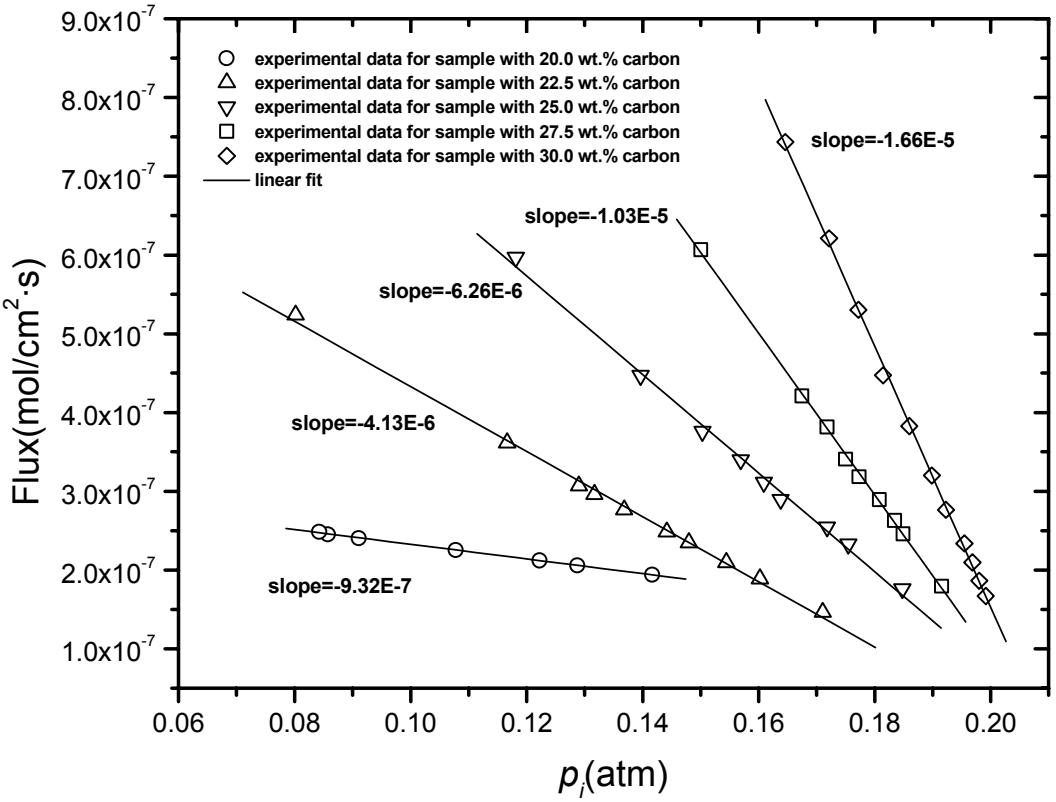

Figure 4. Oxygen flux through porous LSM discs fabricated with varying amounts of carbon, between 20.0 wt.% and 30.0 wt.%, as a function of oxygen partial pressure inside the cell. Measurement conducted at 800^{o}C.

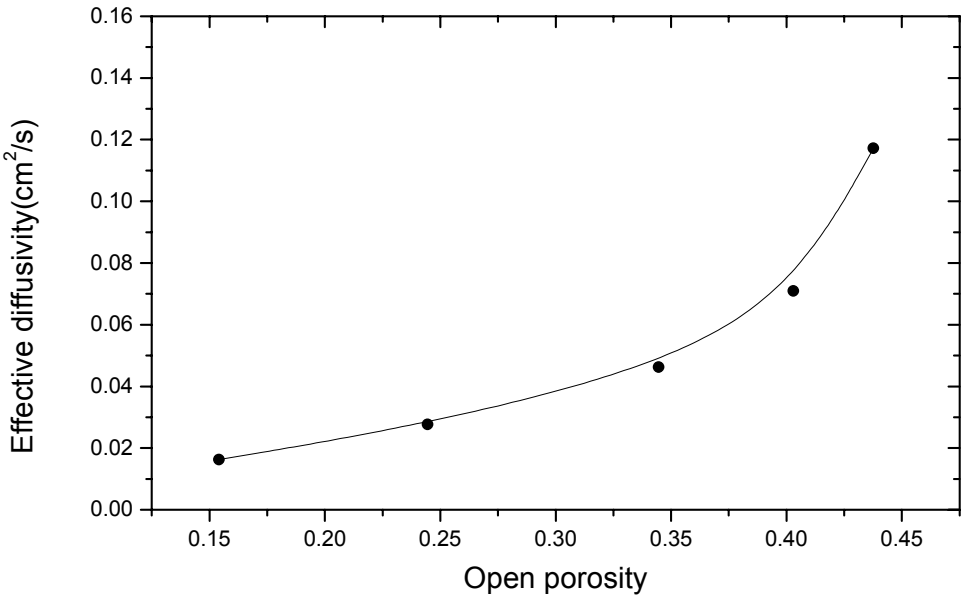

Figure 5. Effective binary diffusivity, $D^{eff}_{O_2-N_2}$, vs. open porosity.

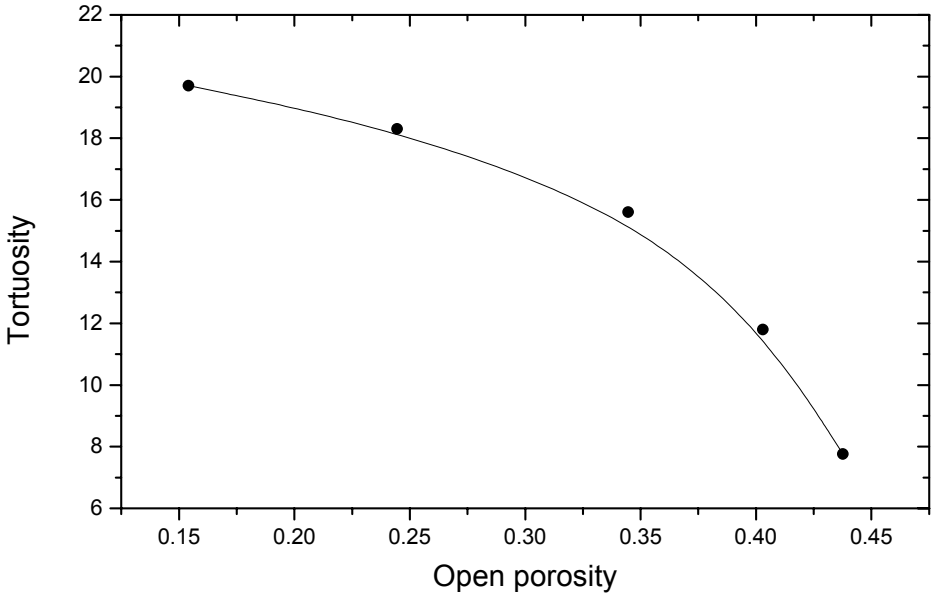

Figure 6. Tortuosity factor vs. open porosity.

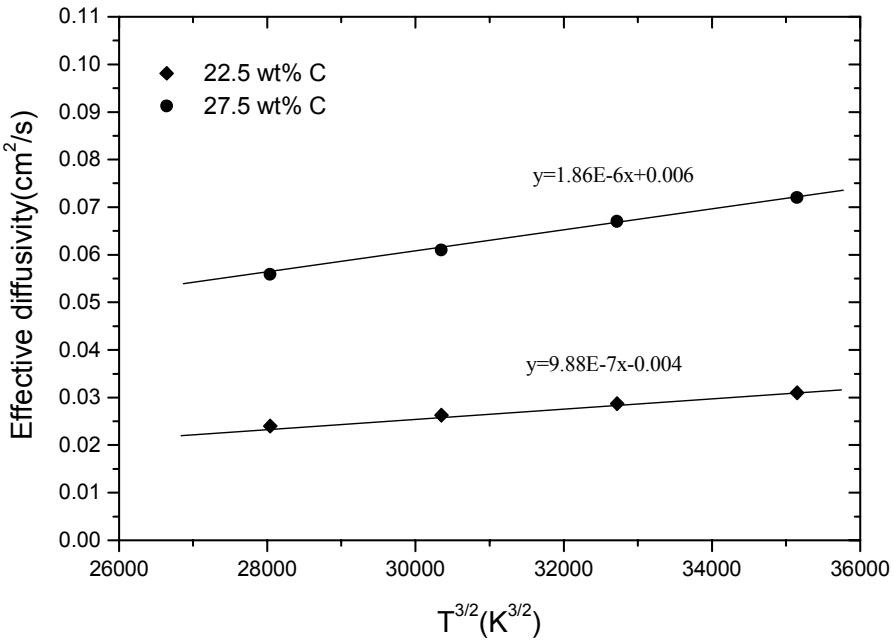

Figure 7. Effective binary diffusivity, $D_{O_2-N_2}^{eff}$, as a function of temperature, $T^{1.5}$, for porous LSM disks fabricated with 22.5 and 27.5 wt.% carbon.

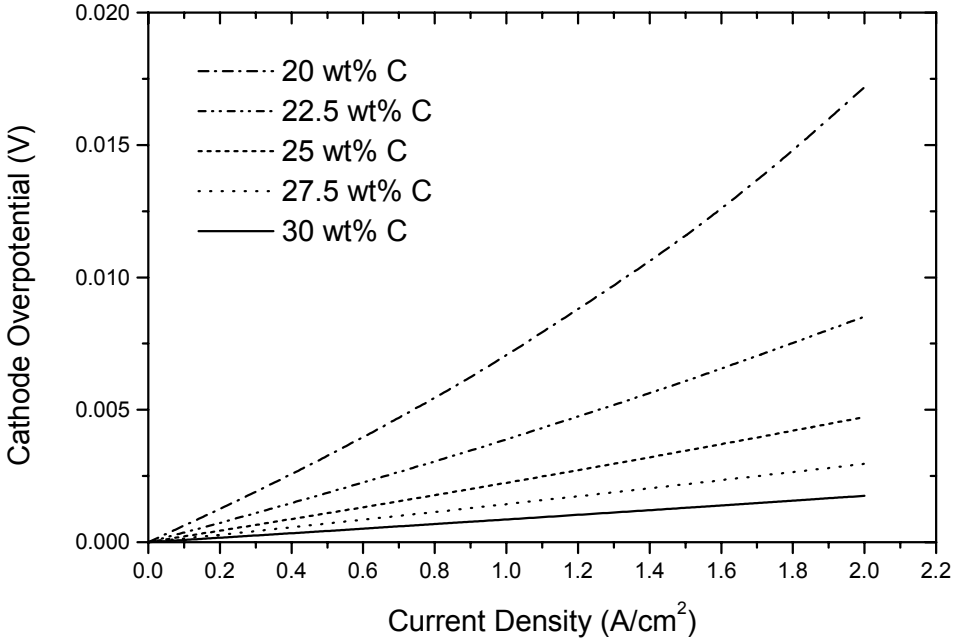

Figure 8(a). Calculated cathode overpotential as a function of current density for porous LSM cathodes fabricated with 20.0 to 30.0 wt.% carbon. Cathode thickness = 50 microns. Cathode-limiting current density calculated using equation (32).

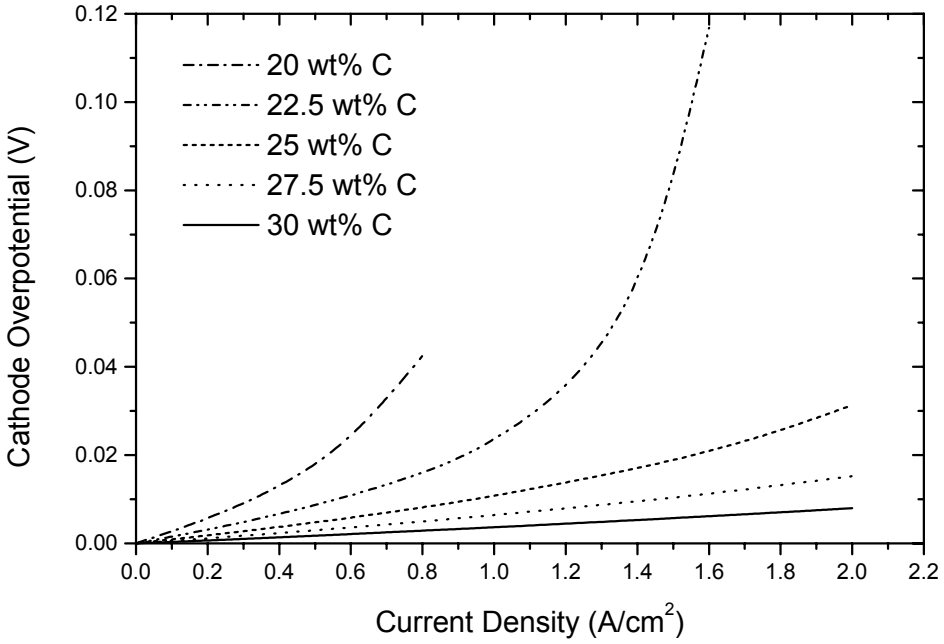

Figure 8(b). Calculated cathode overpotential as a function of current density for porous LSM cathodes fabricated with 20.0 to 30.0 wt.% carbon. Cathode thickness = 200 microns. Cathode-limiting current density calculated using equation (32).

Table I. Density and volume percent of porosity of LSM samples fabricated with various weight percents of carbon.

Weight Percent of Carbon	Density (g/cm^3)	Total Porosity by SEM (vol.%)	Total Porosity (vol.%)	Open Porosity (vol.%)	Closed Porosity (vol.%)	Fraction of Open to Total Porosity
20% C	4.64	26.3	28.89	15.42	13.40	0.53
22.5% C	4.33	32.2	33.69	24.45	9.20	0.72
25% C	3.98	38.5	39.00	34.66	4.30	0.88
27.5% C	3.63	42.2	44.44	40.30	4.10	0.91
30% C	3.41	45.3	47.70	43.77	3.90	0.92

Table II. Measured effective diffusivity, open porosity, tortuosity, and effective O_2 and N_2 Knudsen diffusivity for LSM samples fabricated with various amounts of carbon.

Weight Percent of Carbon	$D^{eff}_{O_2-N_2}$ (cm^2/s) From the slope	$D^{eff}_{O_2-N_2}$ (cm^2/s) From the intercept	Open Porosity	Tortuosity	$D^{eff}_{O_2K}$ (cm^2/s)	$D^{eff}_{N_2K}$ (cm^2/s)
20% C	0.016	0.027	15.42	19.7	0.22	0.235
22.5% C	0.028	0.027	24.43	18.3	0.375	0.401
25% C	0.046	0.046	34.66	15.6	0.624	0.667
27.5% C	0.071	0.07	40.30	11.8	0.959	1.025
30% C	0.117	0.117	43.77	7.8	1.576	1.684

Table III. Measured effective diffusivity as a function of temperature for two LSM disks with different amounts of porosity.

Temperature (^{o}C)	$D^{eff}_{O_2-N_2}$ (cm^2/s)	
	Sample fabricated with 22.5 wt.% C	Sample fabricated with 27.5 wt.% C
650	0.024	0.056
700	0.026	0.062
750	0.029	0.067
800	0.031	0.072

Table IV. Measured effective diffusivity, open porosity and cathode limiting current density for LSM disks fabricated with various amounts of carbon.

Sample	$D_{O_2-N_2}^{eff}$ (cm^2/s)	Open Porosity (%)	i_{cs} (50 μm)* (A/cm^2)	i_{cs} (50 μm)$ (A/cm^2)	i_{cs} (200 μm)* (A/cm^2)	i_{cs} (200 μm)$ (A/cm^2)
1 (20% C)	0.016	15.42	3.37	3.8	0.84	0.95
2 (22.5% C)	0.028	24.43	5.73	6.46	1.43	1.61
3 (25% C)	0.046	34.66	9.55	10.77	2.38	2.69
4 (27.5% C)	0.071	40.30	14.66	16.53	3.66	4.13
5 (30% C)	0.117	43.77	24.24	27.33	6.05	6.83

* Calculated using equation (32).
$ Calculated using equation (33).

Table V. Calculated cathode overpotential at different cathode thickness for LSM samples fabricated with various amounts of carbon at a current density of 2 A/cm^2.

Thickness (μm)	20 wt.% C Cathode overpotential (mV)	22.5 wt.% C Cathode overpotential (mV)	25 wt.% C Cathode overpotential (mV)	27.5 wt.% C Cathode overpotential (mV)	30 wt.% C Cathode overpotential (mV)
50	7.1	3.9	2.3	1.4	0.9
100	17.3	8.6	4.8	3.0	1.8
150	36.1	14.5	7.6	4.6	2.7
200	86.2	22.4	10.8	6.4	3.7